Simulating cosmic rays in clusters of galaxies – I. Effects on the Sunyaev-Zel'dovich effect and the X-ray emission

C. Pfrommer,[1][★] T. A. Enßlin,[2][★] V. Springel,[2][★] M. Jubelgas,[2][★] K. Dolag[2][★]

[1]*Canadian Institute for Theoretical Astrophysics, University of Toronto, 60 St. George Street, Toronto, Ontario, M5S 3H8, Canada*
[2]*Max-Planck-Institut für Astrophysik, Karl-Schwarzschild-Straße 1, Postfach 1317, 85741 Garching, Germany*

11 April 2007

ABSTRACT

We performed high-resolution simulations of a sample of 14 galaxy clusters that span a mass range from $5 \times 10^{13} h^{-1}\,\mathrm{M}_\odot$ to $2 \times 10^{15} h^{-1}\,\mathrm{M}_\odot$ to study the effects of cosmic rays (CRs) on thermal cluster observables such as X-ray emission and the Sunyaev-Zel'dovich effect. We analyse the CR effects on the intra-cluster medium while simultaneously taking into account the cluster's dynamical state as well as the mass of the cluster. The modelling of the cosmic ray physics includes adiabatic CR transport processes, injection by supernovae and cosmological structure formation shocks, as well as CR thermalization by Coulomb interaction and catastrophic losses by hadronic interactions. While the relative pressure contained in CRs within the virial radius is of the order of 2 per cent in our non-radiative simulations, their contribution rises to 32 per cent in our simulations with dissipative gas physics including radiative cooling, star formation, and supernova feedback. The relative CR pressure rises towards the outer regions due to a combination of the following effects: CR acceleration is more efficient at the peripheral strong accretion shocks compared to weak central flow shocks, adiabatic compression of a composite of CRs and thermal gas disfavours the CR pressure relative to the thermal pressure due to the softer equation of state of CRs, and CR loss processes are more important at the dense centres. Interestingly, in the radiative simulations the relative CR pressure reaches high values of the order of equipartition with the thermal gas in each cluster galaxy due to the fast thermal cooling of gas which diminishes the thermal pressure support relative to that in CRs. This also leads to a lower effective adiabatic index of the composite gas that increases the compressibility of the intra-cluster medium. This effect slightly increases the central density, thermal pressure and the gas fraction. While the X-ray luminosity in low mass cool core clusters is boosted by up to 40 per cent, the integrated Sunyaev-Zel'dovich effect appears to be remarkably robust and the total flux decrement only slightly reduced by typically 2 per cent. The resolved Sunyaev-Zel'dovich maps, however, show a larger variation with an increased central flux decrement.

Key words: radiation mechanisms: general – cosmic rays – galaxies: cluster: general – cooling flows – large-scale structure of Universe – X-rays: galaxies: clusters

1 INTRODUCTION

Cosmic ray protons (hereafter referred to as CRs) play a decisive role within the interstellar medium of our own Galaxy. CRs and magnetic fields each contribute roughly as much energy and pressure to the galactic ISM as the thermal gas does, CRs trace past energetic events such as supernovae, and they reveal the underlying structure of the baryonic matter distribution through their interactions. In contrast, it is unknown how much pressure support is pro-

vided by CRs to the thermal plasma of clusters of galaxies. A substantial CR pressure contribution might have a major impact on the properties of the intra-cluster medium (ICM) and potentially modify thermal cluster observables such as the X-ray emission and the Sunyaev-Zel'dovich (SZ) effect (Sunyaev & Zeldovich 1972). This effect arises since photons from the cosmic microwave background experience inverse Compton up-scattering by thermal electrons of the ICM. CR induced modifications might imprint themselves in changes of cluster scaling relations or modify their intrinsic scatter and thus change the effective mass threshold of X-ray or SZ surveys. Neglecting such a CR component in reference simulations might introduce biases in the determination of cosmological parameters. Finally, simulating realistic CR distributions within galaxy clusters enables us to predict the non-thermal cluster emission re-

sulting from CR interactions with thermal gas protons. The result-
ing model signatures of the expected radio synchrotron and γ-ray
emission can then be tested with the upcoming new generation of
γ-ray instruments (e.g. imaging atmospheric Čerenkov telescopes
and the GLAST[1] satellite) and radio telescopes (e.g. LOFAR[2] and
extended Very Large Array[3]).

A thorough dynamical treatment of CR transport and loss pro-
cesses in numerical simulations of cosmological large-scale struc-
ture formation has not yet been attempted due to the very complex
CR physics involved, despite the potential dynamical importance of
CRs. There have been pioneering efforts to study the CR acceler-
ation into the intergalactic medium (IGM) on large scales (Miniati
et al. 2001; Kang et al. 2002; Ryu & Kang 2003, 2004; Kang &
Jones 2005). However, these codes were quite limited in their adap-
tive resolution capability and neglected dissipative gas physics in-
cluding radiative cooling, star formation, and supernova feedback.
There have also been numerical modelling of discretised CR en-
ergy spectra on top of grid-based cosmological simulations (Miniati
2001), but so far these implementations neglected the hydrody-
namic pressure of the CR component and were unable to resolve
the observationally accessible, dense central regions of clusters.

First important results underscoring the importance of CR
populations in clusters were obtained in non-radiative cosmolog-
ical simulations and predicted relative CR pressure contributions
of $P_{CR}/P_{th} \sim 20$ per cent up to 50 per cent (Miniati et al. 2001),
which also motivated suggestions that CRs may slow-down clus-
ter cooling flows (Cen 2005). Since the CR acceleration depends
crucially on the shock strength of cosmological structure forma-
tion shocks, there has been a series of efforts undertaken to develop
schemes that are capable of measuring the Mach numbers in cos-
mological simulations (Miniati et al. 2000; Ryu et al. 2003; Pfrom-
mer et al. 2006). To allow studies of the dynamical effects of CRs
in radiatively cooling galactic and cluster environments, we have
developed a CR formalism that is based on smoothed particle hy-
drodynamical representation of the equations of motion. We intro-
duced a number of approximations to reduce the complexity of the
problem while still being able to capture as many physical proper-
ties and peculiarities of CR populations as possible. In our model,
the emphasis is given to the dynamical impact of CRs on hydrody-
namics, and not on an accurate spectral representation of the CRs.
The guiding principles are energy, pressure, and particle number
conservations, as well as adiabatic invariants. Non-adiabatic pro-
cesses are mapped onto modifications of these principles (Enßlin
et al. 2006; Jubelgas et al. 2006; Pfrommer et al. 2006).

A simplified overview over the relevant physical processes in
galaxy clusters is given in Fig. 1. The *upper central part* shows
standard processes which are usually considered in simulations.
Radiative cooling of the gas leads eventually to star formation in the
densest regions that exceed a certain density threshold. This hap-
pens in the central cluster regions and within substructures leading
to individual galaxies. Once the nuclear energy has been used up,
massive stars explode in supernovae that drive strong shock waves
into the ambient interstellar medium (ISM) which resupply thermal
and turbulent energy. On larger scales, structure formation shock
waves dissipate gravitational energy associated with hierarchical
clustering into thermal energy of the gas, thus supplying the intra-
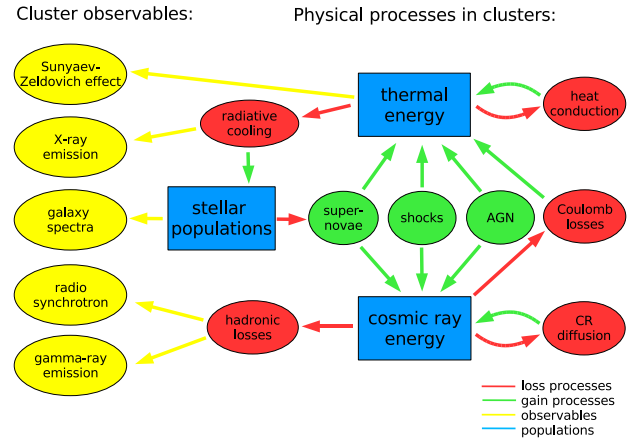cluster medium (ICM) with entropy and thermal pressure support.

Figure 1. Overview over the relevant physical processes in galaxy clus-
ters. The right-hand side shows the interplay of different physical processes
while the left-hand side shows observables that inform about the properties
of cluster and their dynamical state. Gain processes are denoted in green
and loss respectively redistribution processes are denoted in red.

There are three main observables associated with these processes:
the hot ICM emits thermal bremsstrahlung radiation with an X-
ray luminosity that depends on the square of the electron number
density. The amplitude of the Sunyaev-Zel'dovich effect (Sunyaev
& Zeldovich 1972) depends on the pressure of the thermal electron
population integrated along the line-of-sight through the cluster. Fi-
nally, galaxy spectra probe directly the stellar populations of intra-
cluster galaxies and indirectly the cluster's potential through their
velocity dispersion (for reviews see Sarazin 1988; Voit 2005).

The *lower part* of Fig. 1 sketches the cosmic ray physics
within clusters. CRs behave differently compared to the thermal
gas. Their equation of state is softer, they are able to travel actively
over macroscopic distances, and their energy loss time-scales are
typically larger than the thermal ones. Besides thermalization, col-
lisionless shocks are also able to accelerate ions of the high-energy
tail of the Maxwellian through diffusive shock acceleration (for re-
views see Drury 1983; Blandford & Eichler 1987; Malkov & O'C
Drury 2001). These energetic ions are reflected at magnetic irregu-
larities through magnetic resonances between the gyro-motion and
waves in the magnetised plasma and are able to gain energy in mov-
ing back and forth through the shock front. This acceleration pro-
cess typically yields a cosmic ray proton (CR) population with a
power-law distribution of the particle momenta. CRs are acceler-
ated on galactic scales through supernova shocks while they are
injected by structure formation shock waves on even larger scales
up to tens of Mpc.

The ubiquitous cosmic magnetic fields couple the otherwise
dynamically independent ingredients like the ICM plasma, and the
CR gas into a single, however complex fluid. Magnetic fields pre-
vent charged relativistic particles to travel macroscopic distances
with their intrinsic velocity close to the speed of light. Instead,
the particles gyrate around, and travel slowly along magnetic field
lines. Occasionally, they get scattered on magnetic irregularities.
On macroscopic scales, the transport can often be described as a
diffusion process if the gyro-radius can be regarded to be small.
Thus, CR diffusion redistributes the CR energy density macroscop-
ically. Thermal heat conduction is an analogous process that real-
locates the thermal energy of the ICM. The CR energy reservoir

suffers two main loss processes: (1) CR energy is transferred into the thermal energy reservoir through individual electron scatterings in the Coulomb field of the CR particle as well as by small momentum transfers through excitations of quantised plasma oscillations. We refer to the sum of both effects as Coulomb losses. (2) Provided the CR momentum exceeds the threshold $p \simeq 0.8\,\mathrm{GeV}/c$ for the hadronic reaction with ambient protons, they produce pions which decay into secondary electrons (and neutrinos) and γ-rays:

$$\pi^{\pm} \rightarrow \mu^{\pm} + \nu_{\mu}/\bar{\nu}_{\mu} \rightarrow e^{\pm} + \nu_e/\bar{\nu}_e + \nu_{\mu} + \bar{\nu}_{\mu}$$
$$\pi^0 \rightarrow 2\gamma.$$

Only CR protons above this kinematic threshold are therefore visible through their decay products via radiative processes, making them directly observationally detectable. These hadronically produced relativistic electrons and positrons can emit a halo of radio synchrotron emission in the presence of ubiquitous intra-cluster magnetic fields. However, there are other processes that accelerate relativistic electrons such as resonant and non-resonant interactions of mildly relativistic electrons with magneto-hydrodynamic waves or turbulent spectra. Since the distribution of magnetic field strengths with cluster radius is also not well known, radio synchrotron emission alone has limited predictive power. Future γ-ray satellites should be able to detect the associated hadronically induced γ-ray emission resulting from neutral pion decay and allow stronger conclusions on the parent CR population in clusters.

So far, we have neglected feedback from active galactic nuclei (AGN) in our simulations despite its importance (for first models of the thermal feedback within cosmological simulations, see Sijacki & Springel 2006). Gravitational energy associated with the accretion onto super-massive black holes is converted into large-scale jets and eventually dissipated into thermal and CR energy. A reliable model would be required to self-regulate and respond to the instantaneous cooling rate.

This paper studies the interplay of thermal gas and CRs and their effect on the observables of the thermal gas such as X-ray emission and the Sunyaev-Zel'dovich effect. Two companion papers are studying directly the CR related multi-frequency observables and the systematic bias and scatter of cluster scaling relations that are associated with CRs and how these modifications effect the determination of cosmological parameters. The outline of the paper is as follows. Section 2 describes the general setup of the simulations, the different physical processes which we simulated, and our cluster sample. In Sect. 3, we present the results on the relative CR pressure integrated over the clusters, and show the profiles of thermodynamical and CR-related quantities separately for non-radiative and radiative simulations. Both types of simulation models will be concluded by an emerging picture of CR-induced changes to the ICM. Section 3.4 analyses physical processes related to CRs in detail and complements the previous section. Finally, Sect. 3.5 studies the consequences of these processes for thermal observables such as X-ray emission and the Sunyaev-Zel'dovich effect.

2 THE SIMULATIONS

2.1 General setup

Simulations were performed using the "concordance" cosmological cold dark matter model with a cosmological constant (ΛCDM). The cosmological parameters of our model are: $\Omega_m = \Omega_{DM} + \Omega_b = 0.3$, $\Omega_b = 0.039$, $\Omega_\Lambda = 0.7$, $h = 0.7$, $n = 1$, and $\sigma_8 = 0.9$. Here, Ω_m

denotes the total matter density in units of the critical density for geometrical closure today, $\rho_{crit} = 3H_0^2/(8\pi G)$. Ω_b and Ω_Λ denote the densities of baryons and the cosmological constant at the present day. The Hubble constant at the present day is parametrized as $H_0 = 100\,h\,\mathrm{km\,s^{-1}Mpc^{-1}}$, while n denotes the spectral index of the primordial power-spectrum, and σ_8 is the *rms* linear mass fluctuation within a sphere of radius $8\,h^{-1}\mathrm{Mpc}$ extrapolated to $z = 0$. This model yields a reasonable fit to current cosmological constraints.

Our simulations were carried out with an updated and extended version of the distributed-memory parallel TreeSPH code GADGET-2 (Springel 2005; Springel et al. 2001) that includes self-consistent cosmic ray physics (Enßlin et al. 2006; Jubelgas et al. 2006; Pfrommer et al. 2006). Gravitational forces were computed using a combination of particle-mesh and tree algorithms. Hydrodynamic forces are computed with a variant of the smoothed particle hydrodynamics (SPH) algorithm that conserves energy and entropy where appropriate, i.e. outside of shocked regions (Springel & Hernquist 2002).

We have performed high-resolution hydrodynamic simulations of the formation of 14 galaxy clusters. The clusters span a mass range from $5 \times 10^{13}\,h^{-1}\,\mathrm{M_\odot}$ to $2 \times 10^{15}\,h^{-1}\,\mathrm{M_\odot}$ and have originally been selected from a low-resolution dark-matter- (DM)-only simulation (Yoshida et al. 2001) with box-size $479\,h^{-1}\,\mathrm{Mpc}$ of a flat ΛCDM model with the parameters mentioned above. Using the 'zoomed initial conditions' technique (Katz & White 1993; Tormen et al. 1997), we then re-simulated the clusters with higher mass and force resolution by adding short-wavelength modes within the Lagrangian regions in the initial conditions that will evolve later-on into the structures of interest (using initial conditions from Dolag et al. 2005). In these high-resolution regions, dark matter particles of the parent simulation are split into a dark matter and gaseous part, with the mass ratio reflecting the value of the cosmic baryon fraction. Force and mass resolution are then gradually degraded in regions larger than at least 3-5 virial radii from the clusters to limit the computational cost while providing a correct representation of the large scale tidal gravitational field. Using an iterative method, the size of the cluster region that is re-simulated at high-resolution was always chosen to be large enough to prevent any contamination with heavy dark matter particles.

In high-resolution regions, the dark matter particles had masses of $m_{DM} = 1.13 \times 10^9\,h^{-1}\,\mathrm{M_\odot}$ and SPH particles $m_{gas} = 1.7 \times 10^8\,h^{-1}\,\mathrm{M_\odot}$ so each individual cluster is resolved by 8×10^4 to 4×10^6 particles, depending on its final mass. For details of cluster properties, see Sect. 2.3. The SPH densities were computed from 48 neighbours, allowing the SPH smoothing length to drop at most to half of the value of the gravitational softening length of the gas particles. This choice of the SPH smoothing length leads to our minimum gas resolution of approximately $8 \times 10^9\,h^{-1}\,\mathrm{M_\odot}$. For the initial redshift we chose $1 + z_{init} = 60$. The gravitational force softening was of a spline form (e.g., Hernquist & Katz 1989) with a Plummer equivalent softening length that is assumed to have a constant comoving scale down to $z = 5$, and a constant value of $5\,h^{-1}\mathrm{kpc}$ in physical units at later epochs.

2.2 The models

For each galaxy cluster we ran six different simulations separated into two sets of three simulations each (cf. Table 1). One set uses only non-radiative gas physics while the other set consists of three simulations that include radiative cooling and star formation. The first simulation of the non-radiative set is our reference simulation with non-radiative physics only, i.e. the gas is transported adiabat-

Table 1. : D   :

Simulated physics[1]	non-radiative simulation models[1]:			radiative simulation models[1]:		
	reference mod.	shock-CR mod.	simple shock-CR mod.	reference mod.	shock-CR mod.	complete CR mod.
thermal shock heating	✓	✓	✓	✓	✓	✓
radiative cooling				✓	✓	✓
star formation				✓	✓	✓
Coulomb CR losses		✓	✓		✓	✓
hadronic CR losses		✓	✓		✓	✓
shock-CRs with $\zeta = $ const[2]			✓			
shock-CRs with $\zeta(\mathcal{M})$[2]		✓			✓	✓
supernova-CRs						✓

N   :

(1) This table serves as an overview over our simulated models. The first column shows the simulated physics, the next three columns specify our non-radiative simulation models, while the last three columns show our radiative simulation models.

(2) We employ two different CR injection schemes at structure formation shocks: The realistic one uses a Mach number dependent energy injection efficiency $\zeta(\mathcal{M})$ while the simplified scheme uses a constant energy injection efficiency, $\zeta = $ const. The latter scheme is a simplification that exaggerates the CR effects for better visibility. For further details and references please refer to Sec. 2.2.

ically unless it experiences structure formation shock waves that supply the gas with entropy and thermal pressure support. The second simulation of the set allows for a simplified model of CR acceleration at structure formation shocks with a constant energy injection efficiency of $\zeta = \varepsilon_{\mathrm{CR,inj}}/\varepsilon_{\mathrm{diss}} = 0.5$, independent of the shock strength, while reducing at the same time the amount of thermal dissipation to ensure energy conservation at the shock. Here, $\varepsilon_{\mathrm{CR,inj}}$ denotes the injected CR energy density and $\varepsilon_{\mathrm{diss}}$ the total dissipated energy at the shock. This model represents an extreme simplification that exaggerates the CR effects for better visibility. All CR models include Coulomb and hadronic loss processes. The third simulation of the non-radiative set uses a more realistic model for the CR acceleration at structure formation shocks which is based on the thermal leakage model (e.g., Ellison & Eichler 1984; Kang & Jones 1995; Enßlin et al. 2006). It employs the fact that the most energetic ions in the exponential tail of the Maxwellian of the post-shock regime are able to participate in the process of diffusive shock acceleration and injects a power-law in momentum that depends on the instantaneous shock strength in the simulation (for details, cf. Pfrommer et al. 2006). With this thermal leakage model, we are able to derive a CR energy injection efficiency, $\zeta(\mathcal{M})$, for the diffusive shock acceleration process. It depends only on the Mach number of the shock, $\mathcal{M} = v_{\mathrm{s}}/c_1$ (shock velocity v_{s} divided by pre-shock sound speed c_1), the post-shock temperature T_2, and a saturation value of the CR energy injection efficiency at high values of the Mach number, $\zeta_{\mathrm{max}} = 0.5$ as shown in Fig. 2 (Ryu et al. 2003; Enßlin et al. 2006).

The first simulation of our radiative set is a reference simulation with radiative cooling and star formation, but no CR physics. The second radiative simulation accounts for CR acceleration at structure formation shocks and allows for all CR loss processes. Finally, the last simulation additionally assumes that a constant fraction $\zeta_{\mathrm{SN}} = 0.3$ of the kinetic energy of a supernova ends up in the CR population, which is motivated by TeV γ-ray observations of a supernova remnant that find an energy fraction of $\zeta_{\mathrm{SN}} \simeq 0.1 - 0.3$ when extrapolating the CR distribution function (Aharonian & et al. 2006). We choose a maximum value for this supernova energy efficiency owing to the large uncertainties and our aim to bracket the realistic case with the two radiative CR simulations.

Radiative cooling was computed assuming an optically thin gas of primordial composition (mass-fraction of $X = 0.76$ for hydrogen and $1 - X = 0.24$ for helium) in collisional ionisation
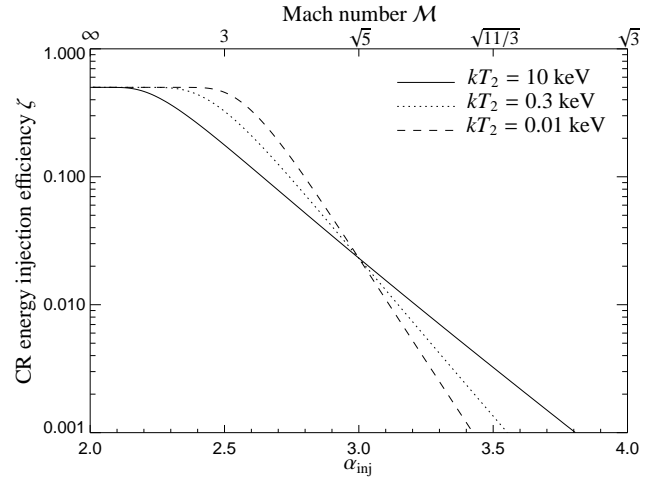

Figure 2. CR energy injection efficiency for the diffusive shock acceleration process. Shown is the CR energy injection efficiency $\zeta = \varepsilon_{\mathrm{CR,inj}}/\varepsilon_{\mathrm{diss}}$ for the three post-shock temperatures $kT_2/\mathrm{keV} = 0.01, 0.3$, and 10. For this illustrative figure, we consider only CRs above the kinematic momentum threshold $q_{\mathrm{threshold}} = p_{\mathrm{CR}}/(m_{\mathrm{p}}c) = 0.83$ of the hadronic CR p-p interaction which are able to produce pions that successively decay into secondary electrons, neutrinos, and γ-rays. We choose equipartition between injected CR energy and dissipated thermal non-relativistic energy as plausible saturation value of the CR energy injection efficiency, i.e. $\zeta_{\mathrm{max}} = 0.5$ (Ryu et al. 2003; Enßlin et al. 2006).

equilibrium, following Katz et al. (1996). We have also included heating by a photo-ionising, time-dependent, uniform ultraviolet (UV) background expected from a population of quasars (Haardt & Madau 1996), which reionizes the Universe at $z \simeq 6$. The effect of a photo-ionising background is that of preventing the collapse of overdense regions of gas and inhibiting subsequent star formation within halos of sub-L_* galaxies (e.g., Benson et al. 2002), thus having a secondary effect on the resolution of our simulation. If not counteracted by any feedback process, radiative cooling in high-resolution simulations is well known to give rise to a central cooling flow that overproduces the amount of stars not only in the group/cluster overdense environment but also in the average environment (e.g., Balogh et al. 2001; Borgani et al. 2004, 2006, and references therein). As discussed by Springel & Hernquist (2003),

their multiphase ISM model with supernovae feedback alone does however not fully resolve this problem, despite its ability to regulate the consumption of cold gas into stars within the ISM. The reason for this is because the cooling rates within halos remain essentially unaffected in the model, i.e. the supply of gas to the dense star-forming ISM is largely unchanged, while by construction the phases of the ISM remain coupled to each other, preventing baryons to leave the ISM (except for dynamical effects like gas stripping in mergers). Being mainly interested in global properties of the ICM, we do not include the metallicity effect in the cooling function due both to the approximate treatment of metal generation and diffusion and in order not to exaggerate the cooling problem of the cluster cores since we also do not follow the AGN feedback that seems to be essential to reliably model the dense cluster centres (e.g., Sijacki & Springel 2006).

Star formation is treated using the hybrid multiphase model for the interstellar medium introduced by Springel & Hernquist (2003). In short, the ISM is pictured as a two-phase fluid consisting of cold clouds that are embedded at pressure equilibrium in an ambient hot medium. The clouds form from the cooling of high density gas, and represent the reservoir of baryons available for star formation. When stars form, according to a Salpeter initial mass function (IMF) (Salpeter 1955), the energy released by supernovae heats the ambient hot phase of the ISM, and in addition, clouds in supernova remnants are evaporated. These effects establish a tightly self-regulated regime for star formation in the ISM. In practice, the scheme is numerically implemented as a sub-resolution model, i.e. cold clouds are not resolved individually. Instead, only their total mass fraction in each element of the ISM is computed, otherwise they are treated in a stochastic fashion with their collective effect on the ISM dynamics being described by an effective equation of state. The numerical implementation of this multiphase model describes each gas particle as composed by a hot component, having its own mass and density, and a cold neutral component. The relative amount of these two phases is determined by the local value of gas density and temperature.

Cosmic ray physics was computed by using a new formulation that follows the most important injection and loss processes self-consistently while accounting for the CR pressure in the equations of motion (Enßlin et al. 2006; Jubelgas et al. 2006; Pfrommer et al. 2006). We refer to these papers for a detailed description of the formalism, providing here only a short summary of the model. In our methodology, the non-thermal cosmic ray population of each gaseous fluid element is approximated by a simple power law spectrum in particle momentum, characterised by an amplitude, a low-momentum cut-off, and a fixed slope $\alpha = 2.3$. Adiabatic CR transport processes such as compression and rarefaction, and a number of physical source and sink terms which modify the cosmic ray pressure of each particle are modelled. The most important sources considered are injection by supernovae (in our radiative simulations) and diffusive shock acceleration at cosmological structure formation shocks, while the primary sinks are thermalization by Coulomb interactions, and catastrophic losses by hadronic interactions.

2.3 Simulated clusters

We chose our sample of 14 galaxy clusters such that they span a wide range in mass ($5 \times 10^{13} h^{-1}\,\mathrm{M}_\odot$ to $2 \times 10^{15} h^{-1}\,\mathrm{M}_\odot$) and show a variety of dynamical states ranging from relaxed cool core (CC) clusters to violent merging clusters (cf. Table 2). Since the CR injection crucially depends on the strength of shock waves we expect

Table 2. : C

Cluster	sim.'s	dyn. state[1]	$M_{200}^{(2)}$ [$h^{-1}\mathrm{M}_\odot$]	$R_{200}^{(2)}$ [h^{-1} Mpc]	$kT_{200}^{(3)}$ [keV]
1	g8a	CC	1.8×10^{15}	2.0	13.1
2	g1a	CC	1.3×10^{15}	1.8	10.6
3	g72a	PostM	1.1×10^{15}	1.7	9.4
4	g51	CC	1.1×10^{15}	1.7	9.4
5	g1b	M	3.7×10^{14}	1.2	4.7
6	g72b	M	1.5×10^{14}	0.87	2.4
7	g1c	M	1.4×10^{14}	0.84	2.3
8	g8b	M	1.0×10^{14}	0.76	1.9
9	g1d	M	9.2×10^{13}	0.73	1.7
10	g676	CC	8.8×10^{13}	0.72	1.7
11	g914	CC	8.5×10^{13}	0.71	1.6
12	g1e	M	6.4×10^{13}	0.65	1.3
13	g8c	M	5.9×10^{13}	0.63	1.3
14	g8d	PreM	5.4×10^{13}	0.61	1.2

N :

(1) The dynamical state has been classified through a combined criterion invoking a merger tree study and the visual inspection of the X-ray brightness maps. The labels for the clusters are M–merger, PostM–post merger (slightly elongated X-ray contours, weak cool core region developing), PreM–pre-merger (sub-cluster already within the virial radius), CC–cool core cluster with extended cooling region (smooth X-ray profile).

(2) The virial mass and radius are related by $M_\Delta(z) = \frac{4}{3}\pi \Delta \rho_{\mathrm{crit}}(z) R_\Delta^3$, where $\Delta = 200$ denotes a multiple of the critical overdensity $\rho_{\mathrm{crit}}(z) = 3H(z)^2/(8\pi G)$.

(3) The virial temperature is defined by $kT_\Delta = GM_\Delta \mu\, m_{\mathrm{p}}/(2R_\Delta)$, where μ denotes the mean molecular weight.

the impact of CR effects to depend on both, the cluster size and its dynamical state. To investigate this dependence, we re-simulated three isolated clusters (cluster 4, 10, and 11) and three super-cluster regions which are each dominated by a large cluster (cluster 1, 2, and 3) and surrounded by satellite clusters (cluster 5 to 9 and 12 to 14).

We analysed the clusters with a halo-finder based on spherical overdensity followed by a merger tree analysis in order to get the mass accretion history of the main progenitor. We also produced projections of the X-ray emissivity at redshift $z = 0$ in order to get a visual impression of the cluster morphology. The dynamical state of a cluster is defined by a combined criterion: (i) if the cluster did not experience a major merger with a progenitor mass ratio 1:3 or larger after $z = 0.8$ (corresponding to a look-back time of $\sim 5\,h^{-1}$ Gyr) and (ii) if the visual impression of the cluster's X-ray morphology is relaxed, it was defined to be a cool core cluster. The merging clusters are subdivided into currently merging clusters, pre-mergers that show a merging sub-cluster already within the virial radius, and post-mergers with slightly elongated X-ray contours in combination with a weak cool core region developing. While this classification may not always be unambiguous in individual cases, it provides robust samples of clusters in these different dynamical states. Interestingly, we note that each satellite cluster within our three super-cluster regions shows signs of merging activity, presumably triggered by the high ambient density that is necessary for the development of a super-cluster region.

The spherical overdensity definition of the virial mass of the cluster is given by the material lying within a sphere centred on a local density maximum, whose radial extend R_Δ is defined by the enclosed threshold density condition $M(< R_\Delta)/(4\pi R_\Delta^3/3) = \rho_{\mathrm{thres}}$. We chose the threshold density $\rho_{\mathrm{thres}}(z) = \Delta \rho_{\mathrm{cr}}(z)$ to be a multiple $\Delta =$

Table 3. : V $\langle X_{\mathrm{CR}} \rangle = \langle P_{\mathrm{CR}} \rangle / \langle P_{\mathrm{th}} \rangle$ $E_{\mathrm{CR}}/E_{\mathrm{th}}$:

relative CR quantity	sample[1]	radiative, shock-CRs[2]	radiative, shock- & SNe-CRs[2]	non-radiative, shock-CRs[2]	non-radiative, shock-CRs with $\zeta = \mathrm{const}$[2]
$\langle X_{\mathrm{CR}} \rangle = \langle P_{\mathrm{CR}} \rangle / \langle P_{\mathrm{th}} \rangle$	small CC	0.045	0.216	0.022	0.321
	large CC	0.034	0.068	0.015	0.369
	merger	0.161	0.414	0.022	0.249
	all	0.120	0.321	0.021	0.272
$E_{\mathrm{CR}}/E_{\mathrm{th}}$	small CC	0.083	0.358	0.037	0.541
	large CC	0.057	0.114	0.025	0.609
	merger	0.266	0.684	0.036	0.410
	all	0.199	0.531	0.034	0.449

N   :

(1) The different cluster samples consist of small cool core (CC) clusters (cluster 10, 11), large cool core clusters (cluster 1, 2, 4), merging clusters (other clusters), and all 14 clusters.

(2) The third column derives from our radiative simulations that account only for structure formation CRs while the values of the forth column correspond to the radiative simulations that take additionally supernova CRs into account. The values in the fifth column derive from non-radiative simulations that accelerate CRs at structure formation shocks using a Mach number dependent energy injection efficiency $\zeta(\mathcal{M})$, while the last column derives from the scheme with a constant energy injection efficiency, $\zeta = \mathrm{const}$.

200 of the critical density of the universe $\rho_{\mathrm{cr}}(z) = 3H(z)^2/(8\pi G)$. For a better comparison with observations and reasons laid out in detail by Evrard (2004), we assume a constant $\Delta = 200$ although some treatments employ a time-varying Δ in cosmologies with $\Omega_{\mathrm{m}} \neq 1$ (Eke et al. 1996). In the reminder of the paper, we use the terminology R_{vir} instead of R_{200}.

3 RESULTS

3.1 Relative CR pressure

Which galaxy clusters are mostly affected by CRs? And does cooling and star formation change the generic picture of CRs in clusters? To answer these two questions it is instructive to consider the CR pressure P_{CR} relative to the thermal pressure P_{th} integrated over the cluster. This is a good measure of the importance of dynamical effects of CRs on the ICM. Table 3 shows the volume averaged values for $\langle X_{\mathrm{CR}} \rangle = \langle P_{\mathrm{CR}} \rangle / \langle P_{\mathrm{th}} \rangle$ within the virial radius R_{vir} and the ratio of the CR-to-thermal energy within the galaxy cluster.

The main findings are the following. (1) Among the non-radiative simulations, $\langle X_{\mathrm{CR}} \rangle$ is much smaller ($\langle X_{\mathrm{CR}} \rangle \sim 2$ per cent) in our improved scheme where CRs are accelerated at structure formation shocks using Mach number dependent energy injection efficiency $\zeta(\mathcal{M})$ compared to the simplified scheme where CRs have been injected with a high constant energy injection efficiency of $\zeta = 0.5$. This shows the importance of a Mach number dependent CR injection scheme to study CR effects within the ICM. (2) Neglecting for the moment the simplified scheme, we notice that $\langle X_{\mathrm{CR}} \rangle$ is much larger in our radiative simulations compared to our non-radiative simulations for reasons that will be analysed in the next sections. (3) Among our radiative simulations, the complete model that accounts for CRs from structure formation shocks on large scales and supernova shocks within the ISM of individual galaxies shows a larger relative CR pressure compared to the model that only accounts for structure formation CRs. Note that the complete model opens simply another channel for CR injection. (4) Comparing different dynamical states of clusters, the relative CR pressure contribution is largest in merging clusters, followed by small cool core clusters, and large cool core clusters. Strong merger shock waves efficiently inject CRs at the external cluster

regions and mix the highly CR-enriched intergalactic medium outside clusters with the ICM. An effect that boosts the relative CR pressure during a merger. Weak virialisation shocks traversing the cluster after the merger thermalize random gas motions and yield a decrease of $\langle X_{\mathrm{CR}} \rangle$. (5) The volume averages for X_{CR} are dominated by the outer regions due to the rising profile of X_{CR} with increasing radius. In other words, the absolute value of $\langle X_{\mathrm{CR}} \rangle$ depends on the definition of the virial radius. A larger virial radius $R_{100} > R_{200}$ would thus lead to an increase of $\langle X_{\mathrm{CR}} \rangle$.

The low level of $\langle X_{\mathrm{CR}} \rangle$ in our non-radiative simulations disagrees with the substantially larger predictions of $\langle X_{\mathrm{CR}} \rangle \sim 20$ per cent to 50 per cent by Miniati et al. (2001). This could be due to a number of reasons. Miniati et al. (2000) identified shocks with Mach numbers in the range $4 \lesssim \mathcal{M} \lesssim 5$ as the most important in thermalizing the plasma. In contrast, Ryu et al. (2003) and Pfrommer et al. (2006) found that the Mach number distribution peaks in the range $1 \lesssim \mathcal{M} \lesssim 3$. Since diffusive shock acceleration of CRs depends sensitively on the Mach number (cf. Fig. 2), this implies a more efficient CR injection in the simulations by Miniati et al. (2001). Secondly, CR injection according to the "thermal leakage" model in the implementation of Miniati (2001) has no injection limiter for the saturated stage of non-linear CR acceleration which might have led to an overestimate of the CR injection for strong shocks. Finally, the grid-based cosmological simulations have been performed in a cosmological box of side-length $50\,h^{-1}$ Mpc with a spatial resolution of $200\,h^{-1}$ kpc, assuming an Einstein-de Sitter cosmological model (Miniati et al. 2001). The lack of resolution inside the clusters in the grid-based approach does not allow one to properly resolve the adiabatic compression of the composite of CRs and thermal gas. As a result, on one hand the disfavouring of the CR pressure relative to the thermal pressure upon compression is not accounted for, and on the other hand, this underestimates CR loss processes at the dense cluster centres due the lack of resolution there.

While our simulations have much higher spatial resolution inside clusters and can therefore be expected to be more accurate, one has to be aware of resolution limitations in them as well. This applies especially to the radiative simulations, which are not able to resolve faint cluster galaxies, and are not guaranteed to give already a converged value for the total amount of stars forming in the clus-

ters. Also, we know that simulated clusters exhibit cooling flows that are much stronger than observed in nature, which can amplify effects related to the CR compression and slow infall of ICM gas in the simulated clusters. However, our main purpose in this paper is to study the principle changes in cluster structure brought about by the inclusion of CRs, and our resolution is high enough to answer this question reliably.

Taking into account that the two radiative CR simulations are chosen to bracket the realistic case, we roughly predict a ratio of the CR-to-thermal energy of $E_{CR}/E_{th} = 9$, 20, and 50 per cent for small CC, large CC, and merging clusters. These predictions are in good agreement with CR constraints from gamma-ray and radio observations (Pfrommer & Enßlin 2003, 2004), considering that these authors assumed a constant CR energy density relative to the thermal gas.

3.2 Profiles of non-radiative simulations

Results for the appropriately scaled average profiles of our non-radiative simulations are shown in Fig. 3 only for our sample of small cool core clusters. The main conclusions drawn from this sample are representative for our complete sample, while including the remaining clusters would only increase the cluster to cluster variance of the profiles, primarily due to the non-sphericity (for merging clusters) and the different concentrations (for large cool core clusters). The radial coordinate has been scaled with R_{vir} to allow comparison between differently sized objects. In all plots of the profiles, the error bars represent the standard deviation σ from the sample mean of the indicated subsample of clusters. The colour scheme for the non-radiative profiles is *black* for our reference simulations without CRs, *red* for simulations where CRs are injected only through shock acceleration using Mach number dependent scheme (realistic CR model), and *blue* for simulations where CRs are accelerated at structure formation shocks with a constant injection efficiency $\zeta = 0.5$ (simplified CR model). One should bare in mind that the latter model represents an extreme simplification that exaggerates the CR effects for better visibility.

3.2.1 Density and temperature profiles

The gas density has been scaled with $\Omega_b \rho_{crit}$ while the temperature has been scaled by its virial quantity that is defined by $kT_{vir} = GM_{vir}\mu m_p/(2R_{vir})$, where $\mu = 4/(3X_H+1+4X_H x_e)$ denotes the mean molecular weight, $X_H = 0.76$ is the primordial hydrogen mass fraction, and x_e is the ratio of electron and hydrogen number densities which we dynamically track in our radiative simulations. Both the average density and the temperature profile of our realistic CR model shows only very small differences to our reference simulations. The tendency of the enhanced density and the reduced temperature in our CR simulations is clearly enhanced in our simplified CR model. While the density enhancement is largest in the centre, the decrease of the cluster temperature is larger at the cluster outskirts for reasons that are described below (cf. Sect. 3.2.5).

3.2.2 Pressure and relative CR pressure profiles

The lines without symbols denote the thermal pressure, the ones with symbols the CR pressure. The CR and thermal pressure have been scaled with $P_{vir} = kT_{vir} 200 \Omega_b \rho_{crit}/(\mu m_p)$. Again, there is only a very small difference visible between the thermal pressure of our realistic CR model and our reference simulations. The trend

of a reduced thermal pressure at cluster outskirts and of the increased central pressure is enhanced in our simplified CR model. In the outer regions, the reduced thermal pressure adds up with the CR pressure to the total (thermal) pressure in our reference simulation while the central pressure enhancement reflects the density enhancement. The CR pressure shows a flat central plateau and decreases at $r > 0.1R_{vir}$ outwards less steeply compared to the thermal pressure.

This yields a rising profile for the relative CR pressure throughout the cluster $X_{CR} = P_{CR}/P_{th}$ due to a combination of the following effects: CR acceleration is more efficient at the peripheral strong accretion shocks compared to weak central flow shocks, adiabatic compression of a composite of CRs and thermal gas disfavours the CR pressure relative to the thermal pressure due to the softer equation of state of CRs, and CR loss processes are more important at the dense centres.

3.2.3 Baryon fraction

In our self-consistent CR model (with varying $\zeta(\mathcal{M})$), the central baryon fraction scaled with the universal value $b = f_{bary}(< x)\Omega_m/\Omega_b$ is increased by ~ 10 per cent and reaches the same value at the virial radius of $b = 0.9$ compared to our reference simulation. Note that the baryon fraction is increasing as a function of radius which can be traced back to the different nature of dark matter and gas. The inner slope of the density profile of collisionless dark matter does not show any sign of flattening (Navarro et al. 2004) while the gas profile is cored due to the isotropic hydrodynamic pressure. This yields to an decreasing baryon fraction towards the centre, an effect that has been observed in many works (e.g. Ettori et al. 2006, and references therein).

Remarkably, the baryon fraction in our simplified CR model (with $\zeta = 0.5$) even exceeds unity at intermediate radii and reaches a value at the virial radius of $b = 0.95$. This is mostly due to the enhanced gas compressibility which boosts the density within the central regions.

3.2.4 Effective adiabatic index

When studying the hydrodynamics of a composite of thermal and CR gas, it is appropriate to define an effective microscopic adiabatic index by

$$\gamma_{eff} \equiv \left.\frac{d\log(P_{th}+P_{CR})}{d\log\rho}\right|_S = \frac{\gamma_{th}+\gamma_{CR}X_{CR}}{1+X_{CR}}, \quad (1)$$

where $\gamma_{th} = 5/3$ is the ideal gas value of the ratio of specific heats and the adiabatic exponent of the CR population is defined by

$$\gamma_{CR} \equiv \left.\frac{d\log P_{CR}}{d\log\rho}\right|_S, \quad (2)$$

while the derivative has to be taken at constant entropy S (Enßlin et al. 2006). Depending on the CR momentum distribution function, γ_{CR} can vary between $\gamma_{CR} \to 4/3$ (in the ultra-relativistic limit) to $\gamma_{CR} \to 5/3$ (in the non-relativistic limit). One should not confuse this effective *microscopic* adiabatic index of our composite fluid that enters the hydrodynamic equations and governs the compressibility of the medium with the effective *macroscopic* adiabatic index one can derive from cluster density and pressure profiles by means of $\gamma = d\log P/(d\log r)[d\log\rho/(d\log r)]^{-1}$. If one compressed gas with such an effective *macroscopic* adiabatic index into a spherical cluster that has the appropriate density profile (without
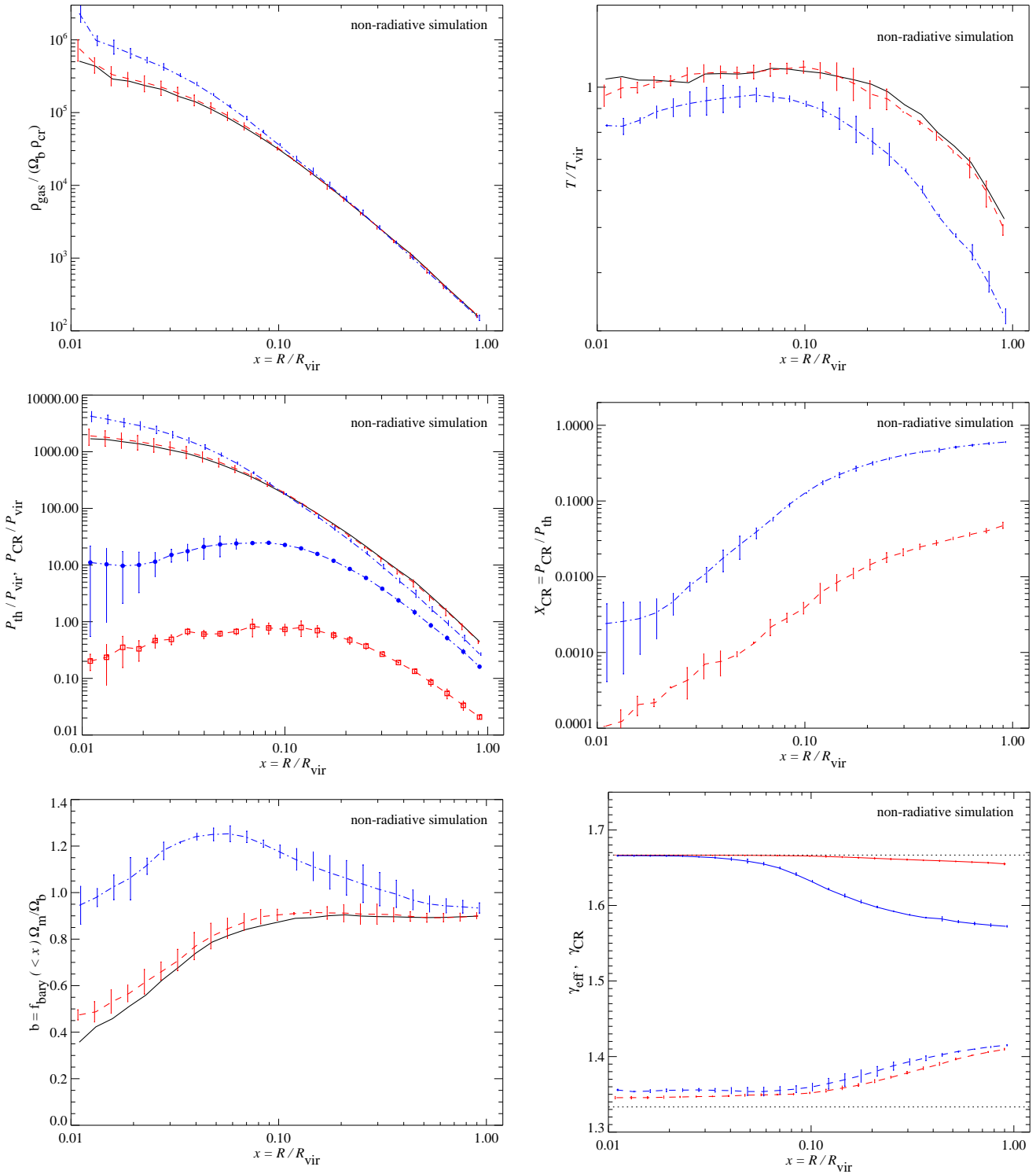
Figure 3. Average profiles of our sample of small cool core clusters (clusters 10, 11) in our non-radiative simulations at redshift $z = 0$. Here and in the following plot, the error bars represent the standard deviation from the sample mean. Shown are the appropriately scaled profiles of the gas density ρ_{gas}, temperature T, thermal and CR pressure (P_{th} and P_{CR}, the latter with symbols), relative CR pressure $X_{CR} = P_{CR}/P_{th}$, baryon fraction b, and the effective adiabatic indices γ_{eff} (solid) in comparison with the CR adiabatic indices γ_{CR} (dashed). Colour scheme: black: reference simulations without CRs, red: CRs are injected only through shock acceleration using our Mach number dependent scheme, blue: CR shock acceleration with constant energy injection efficiency.

considering shocks and cooling), one would obtain the simulated pressure profiles.

The effective adiabatic index γ_{eff} is shown with a solid line while γ_{CR} is shown with a dashed line. As expected, γ_{eff} reflects the profile of X_{CR} and is only different from the adiabatic index $\gamma_{\mathrm{th}} = 5/3$ of the thermal gas in the external cluster regions where CRs make up a larger fraction of the pressure support (in particular in our simplified model). Interestingly, γ_{CR} shows a different behaviour with a slightly softer value in the central cluster regions. This is due to enhanced Coulomb cooling in denser core region which effectively re-thermalizes low-energetic CRs and increases the low momentum cutoff of the CR distribution function. This leads to a more relativistic CR population with a lower CR pressure and thus to the observed behaviour of the adiabatic indices.

3.2.5 Discussion of CRs profiles in non-radiative simulations

Structure formation shock waves propagate through the cosmic tenuous gas, which is compressed at the transition layer of the shock while a part of the kinetic energy of the incoming gas is dissipated into internal energy of the post-shock gas according to the Rankine-Hugoniot jump conditions. Considering CR injection at shocks through diffusive shock acceleration, a part of the energy that has been otherwise completely thermalized is now transferred to the CR energy reservoir while employing energy conservation. This effect lowers the amount of thermalized energy and thus the temperature which is observed at the periphery in clusters (cf. Sect. 3.2.1) where it is most pronounced due to strong shock waves that take place there and inject efficiently CRs (Miniati et al. 2000; Ryu et al. 2003; Pfrommer et al. 2006).

The successive build-up of a cluster profile of thermodynamic variables (such as entropy or pressure) through mergers and mass accretion can be thought of as a combination of two effects. (1) Merger shock waves violently increase the cluster's entropy and (2) permanent accretion of new shells of mass at the peripheral cluster regions exert a pressure that adiabatically compresses the central gas. These two effects have important consequences for the resulting thermal profiles that are modulated by CR pressure. Since CR acceleration is more efficient at the peripheral strong accretion shocks compared to weak central flow shocks, this yields a stratification of the relative CR pressure profile which is increasing outwards. Adiabatic compression of a composite of CRs and thermal gas disfavours the CR pressure relative to the thermal pressure due to the softer equation of state of CRs. Roughly, one expects the ratio of $X_{\mathrm{CR}} = P_{\mathrm{CR}}/P_{\mathrm{th}}$ after adiabatic compression (denoted with a prime) to that before compression to scale as

$$\frac{X'_{\mathrm{CR}}}{X_{\mathrm{CR}}} = \left(\frac{\rho'}{\rho}\right)^{\gamma_{\mathrm{CR}} - \gamma_{\mathrm{th}}} \sim 0.05 \qquad (3)$$

for a compression ratio of $\rho'/\rho \sim 10^4$. Additionally, CR loss processes are more important at the dense cluster centres. Thus, the central density has to increase dynamically in our CR simulation compared to our reference simulations in order to balance the gravitational pressure and make up for the initially 'missing' thermal pressure. Shock heating and adiabatic compression heats the thermal gas in the cluster centre with a higher rate compared to the external regions. Thus, the thermal pressure $P_{\mathrm{th}} = n_{\mathrm{th}} kT$ is increased in the cluster centre in our simulations with CRs compared to our reference simulations without CRs.
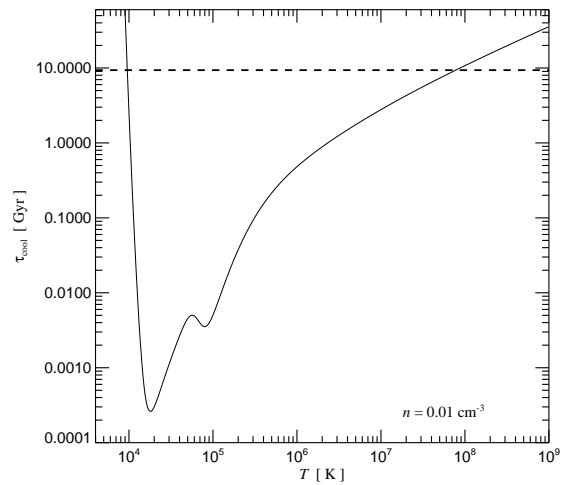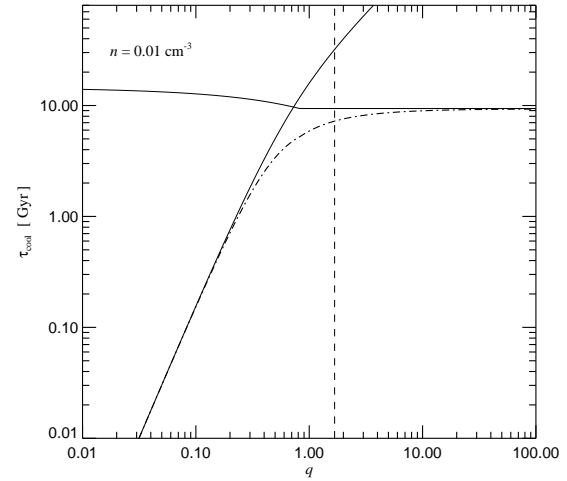

Figure 4. The top panel shows the cooling times due to Coulomb losses (rising solid line) and hadronic dissipation (nearly horizontal line) as a function of the spectral cut-off $q = p_{\mathrm{min}}/(m_{\mathrm{p}}c)$. The dot-dashed line gives the total cooling time, while the vertical dashed lines marks the asymptotic equilibrium cut-off reached by the CR spectrum when no sources are present. The bottom panel shows the cooling time of ordinary thermal gas due to radiative cooling (for primordial metallicity), as a function of temperature. The horizontal dashed line marks the cooling time of CRs with a high momentum cut-off ($q \gg 1$), for comparison. In both panels, the times have been computed for a number density of $n = 0.01\,\mathrm{cm}^{-3}$, a typical number density in the centres of galaxy clusters. Note however that the cooling times all scale as $\tau \propto 1/n$, i.e. for different densities, only the vertical scale would change but the relative position of the lines would remain unaltered.

3.3 Profiles of radiative simulations

The larger CR pressure support in our radiative simulations makes CR related phenomena more pronounced compared to the non-radiative simulations. This crucially depends on the small ratio of the thermal to the comparatively long CR cooling time in regions where the temperature drops below $T \lesssim 10^7$ K. Here, the CR cooling time of an aged CR population with an equipartition value for the lower momentum cutoff $q \sim 1$ remains almost constant, but it decreases for the thermal gas as it is cooling (cf. Fig. 4) and becomes progressively shorter than the CR cooling time. This equipartition value for q results from a balance of Coulomb cooling that increases q and leaves the normalisation of the CR distribution function almost unchanged and CR cooling by hadronic

interactions which decreases the lower momentum cutoff q and the normalisation of the CR distribution function (Jubelgas et al. 2006). Current cosmological radiative simulations that do not include feedback from AGN bubbles (Sijacki & Springel 2006) have an over-cooling problem in the cluster centre where they overproduce the amount of stars. This problem is larger in cool core clusters which did not recently experience a major merger. Compared to X-ray observations, the simulated clusters show enhanced central gas densities, too small central temperatures, too strong central entropy plateaus, and an enhanced baryon fraction that is driven by the large stellar mass fraction towards the cluster centre. These are all manifestations of the cooling flow problem of simulated clusters, an issue that universally occurs in ΛCDM simulations, independent of the employed numerical method (e.g., Borgani et al. 2004; Kravtsov et al. 2005; Ettori et al. 2006).

In our plots of cluster profiles, the error bars represent the standard deviation σ from the sample mean of the indicated subsample of clusters. The error on the mean can easily be obtained by means of $\sigma/\sqrt{N-1}$, where N is the number of clusters in the sample, i.e. $N = 2$ (small CC), $N = 3$ (large CC), $N = 5$ (all CC), $N = 9$ (merging cluster). The colour scheme for the profiles of our radiative simulations is *black* for our reference simulations without CRs, *red* for simulations where CRs are injected only at structure formation shocks using Mach number dependent scheme (*CR-shock model*), and *blue* for the *complete model* that accounts for CR injection from structure formation shocks on large scales (with the Mach number dependent scheme) and supernova shocks within the ISM of individual galaxies with a constant energy injection efficiency of $\zeta_{\mathrm{SN}} = 0.3$. Although our complete model might seem to be more relevant astrophysically, both CR models are chosen to represent extreme cases that are bracketing the realistic scenario in between for the following reasons. The CR-shock model approaches the realistic case from below because it does not take into account CRs from supernova shock waves. Our complete CR model brackets the model from above because it assumes a high CR injection efficiency from supernovae in addition to the too large star formation rate of current radiative simulations. This possibly overestimates the CR energy injection into the ICM in the complete model. After describing the simulated profiles, we synthesise our results in Sect. 3.3.7 and provide further support for our interpretation by considering CR related physical processes in more detail in Sect. 3.4.

3.3.1 Density and temperature profiles

Results for the appropriately scaled average density and temperature profiles of our radiative simulations are shown in Fig. 5. Comparing both CR simulations to our reference simulation, the most striking feature is the density enhancement in the central regions at $r < 0.04\,R_{\mathrm{vir}}$. Our CR-shock model shows a density enhancement at larger radii which is strongest in small cool core clusters and visible up to radii as large as $r = 0.5\,R_{\mathrm{vir}}$. In contrast, our complete model shows a density decrement at intermediate radii that almost disappears in small cool core clusters.

Similarly, the temperature in the central regions is reduced in our CR simulations while it almost coincides at larger radii with our reference simulation. The cluster-to-cluster variance is largest in our merger simulation due to ongoing virialisation processes mediated by structure formation shock waves.

3.3.2 Pressure profiles

Figures 6 and 7 compare profiles of our sample of all cool core clusters (CC clusters, on the left-hand side) to our sample of merging clusters (on the right-hand side). Our samples of small and large CC clusters differ only marginally for these profiles. While the thermal pressure profile of the CC clusters follows a cored β-profile, the pressure profile of merging clusters almost shows a flat single power-law behaviour that is due to the ongoing merging activities (cf. Fig. 6, top panels). The thermal pressure of the CC clusters in our CR-shock model exceeds the one in our reference simulation, while the thermal pressure in the merging clusters shows no significant difference among our different models apart from the innermost central region where we observe an excess in both of our CR models.

In contrast, the CR pressure profiles do not show a core; their profile increases inwards roughly as $P_{\mathrm{CR}} \propto r^{-1}$ up to the external regions of the ISM of the cD galaxy at $r \propto 0.04\,R_{\mathrm{vir}}$, where their profile steepens considerably and scales as $P_{\mathrm{CR}} \propto r^{-2}$ in our CC clusters. The error bars of the CR pressure profiles have been suppressed for clarity. The CR pressure profiles in both of our CR models are similar to each other: the profile in the CR-shock model shows a smoother behaviour while the one in our complete model has a larger radial variation and a higher pressure level due to the additionally injected CR pressure from supernovae within galaxies. The hypothesis that the supernova CRs are irrelevant for the total pressure budget is however inadmissible because simulations that consider only CRs from supernovae shocks show very similar pressure profiles (Jubelgas et al. 2006). The reason lies rather in the fact that any CR population is processed by adiabatic loss and transport processes in a comparable fashion.

3.3.3 Relative CR pressure profiles

It is very instructive to study the relative CR pressure profiles $X_{\mathrm{CR}}(r) = P_{\mathrm{CR}}(r)/P_{\mathrm{th}}(r)$ in Fig. 6, middle panels. Generally, $X_{\mathrm{CR}}(r)$ is larger in merging clusters compared to CC clusters and does not adopt values below $X_{\mathrm{CR}} = 0.1$ at any radius for the complete CR model in merging clusters. As already mentioned in Sect. 3.1, strong merger shock waves efficiently inject CRs at the external cluster regions and mix the highly CR-enriched intergalactic medium outside clusters with the ICM, thus boosting the relative CR pressure during a merger. This also results in large cluster-to-cluster variations at some given radius. Note that the error bars of the relative CR pressure profiles have been suppressed for clarity.

Compared to the very smooth, dynamically unimportant profile of our non-radiative simulations, $X_{\mathrm{CR}}(r)$ shows a steep increase towards the cluster centre within the ISM of the cD galaxy and much larger radial variation in these radiative simulations. This is due to the short thermal cooling time scales within dense galactic environments compared to the comparatively long CR cooling time scales (cf. Fig. 4). There, the thermal gas cools on a small timescale of $\tau \simeq 10^7$ yr, diminishes pressure support, condenses out of the gaseous phase and eventually forms stars. In the process, the CR pressure reaches values that exceed the equipartition with the thermal pressure. In the outer parts of the cluster, $X_{\mathrm{CR}}(r)$ is a rising function with increasing radius due to the same reasons mentioned above in our non-radiative simulations.
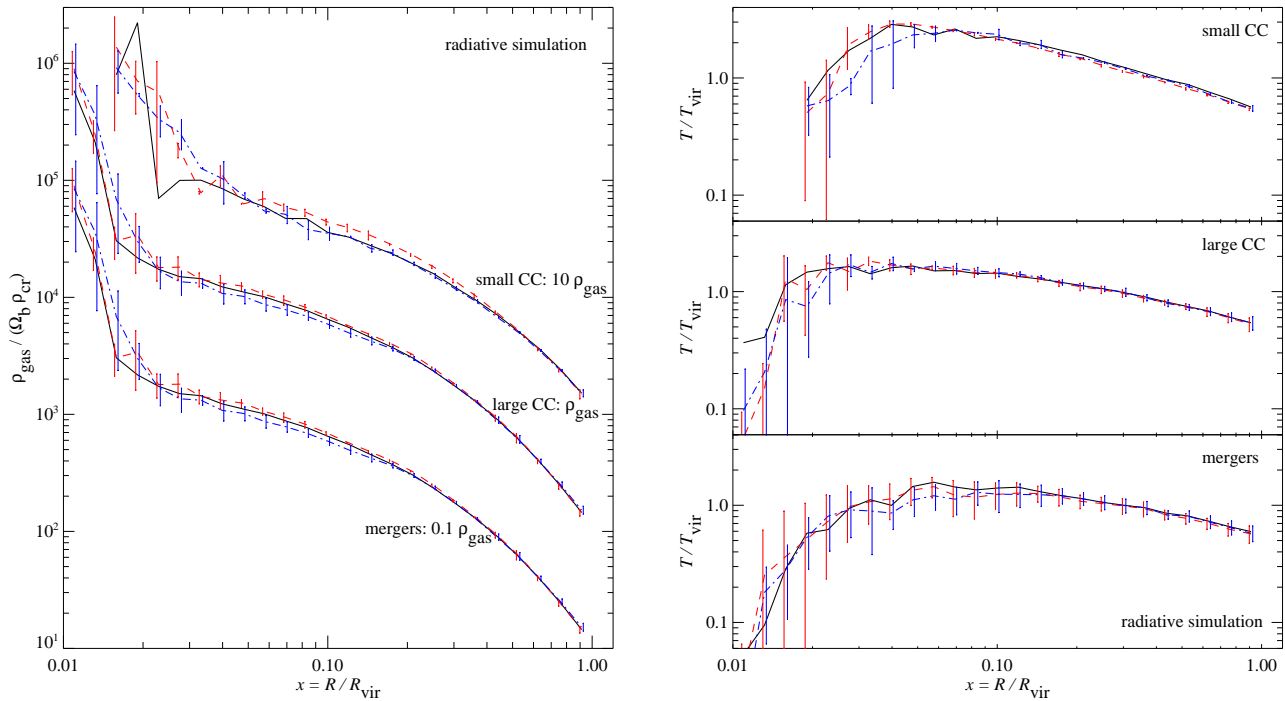
Figure 5. Average profiles of our sample of clusters in our radiative simulations at redshift $z = 0$. Shown are the appropriately scaled profiles of the gas density ρ_{gas} (left-hand side) and temperature T (right-hand side). Colour scheme: black: reference simulations without CRs, red: CRs are injected only through shock acceleration using Mach number dependent scheme, blue: complete CR-model including CR injection from supernovae.

3.3.4 Effective adiabatic index

In our CC cluster sample, the effective adiabatic index γ_{eff} departs from its canonical value $\gamma_{th} = 5/3$ (in the absence of CRs) strongly in the cluster centre inside the ISM of the cD galaxy and at the external regions of the cluster where the relative CR pressure profile is dynamically important (cf. Fig. 6, bottom panels). The composite of CRs and thermal gas acquires there a higher compressibility that requires a larger overdensity in order to exert the same pressure that balances the gravitational pressure from the combination of dark matter and gas. The value of γ_{eff} in our sample of merging clusters is everywhere softer compared to the canonical adiabatic index although there is a large variation among different clusters. This again reflects the higher CR pressure level in merging clusters due to the high CR injection efficiency of merger shock waves.

Interestingly, the adiabatic index of the CR population γ_{CR} in our radiative simulations is harder compared to our non-radiative simulations. This can be traced back to the smaller overdensity in radiative simulations and thus the smaller CR cooling rate due to Coulomb interactions that re-thermalize the low-energy part of the CR momentum distribution function and eventually yield an ultra-relativistic CR population. The lower overdensity in our radiative simulations basically stems from the fact that gas mass from intermediate cluster scales is removed since it replenished the condensing star forming material inside galaxies and most importantly of the central cD galaxy.

3.3.5 Baryon fraction

Figure 7 shows the baryon fraction scaled with the universal value, $b = f_{bary}(< x)\,\Omega_m/\Omega_b$, that reaches values of unity at the virial radius independent of the adopted model and dynamical state of the cluster. The profile of b rises steeply towards the centre, which is mostly due to the increase of the stellar mass fraction relative to the dark matter. Additionally, Fig. 7 shows the gas fraction scaled with the universal value, $f_{gas}(< x)\,\Omega_m/\Omega_b$. Its profile is decreasing inwards in contrast to the scaled baryon fraction. This shows clearly that the stellar mass fraction as well as the stellar mass-to-gas fraction is not constant as a function of radius but strongly increasing inwards. As a word of caution, a fraction of the inward increase of b is caused by the over-cooling problem in the cluster centre where we form too many stars that are too blue compared to observations. We note that this is a result of the well-known cooling flow problem in simulated clusters, which is independent of the employed numerical method (e.g., Borgani et al. 2004; Kravtsov et al. 2005; Ettori et al. 2006, and references therein). CR physics with CR source terms studied in this paper such as structure formation shock waves and supernovae shocks on galactic scales seems to reinforce this problem instead of solving it. Eventually, self-regulating heating sources related to AGNs at cluster centres might be required to solve this problem.

The value of b in our sample of merging clusters is increased by roughly 10 per cent in our CR models compared to our reference simulation while the enhancement is smaller in the CC cluster sample. The simulations show a decreasing gas mass fraction towards the centre for reasons that have been explained in Sect. 3.2.3.

3.3.6 Cumulative stellar mass

The profile of the cumulative stellar mass normalised by the virial mass of the cluster is shown in Fig. 7. One notes that there is a higher fraction of stellar mass formed relative to M_{vir} in our small CC clusters compared to the larger ones. This might be partly due

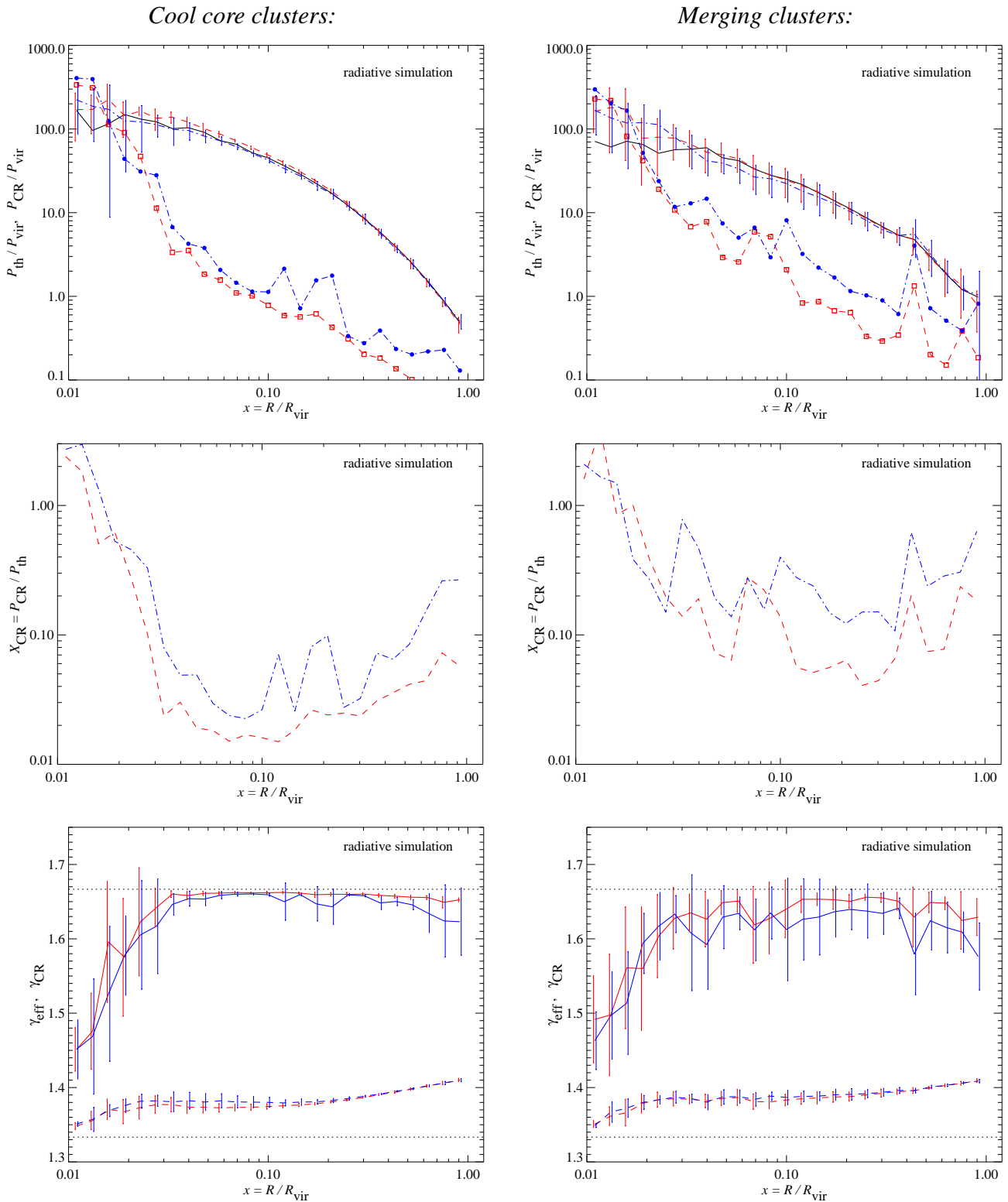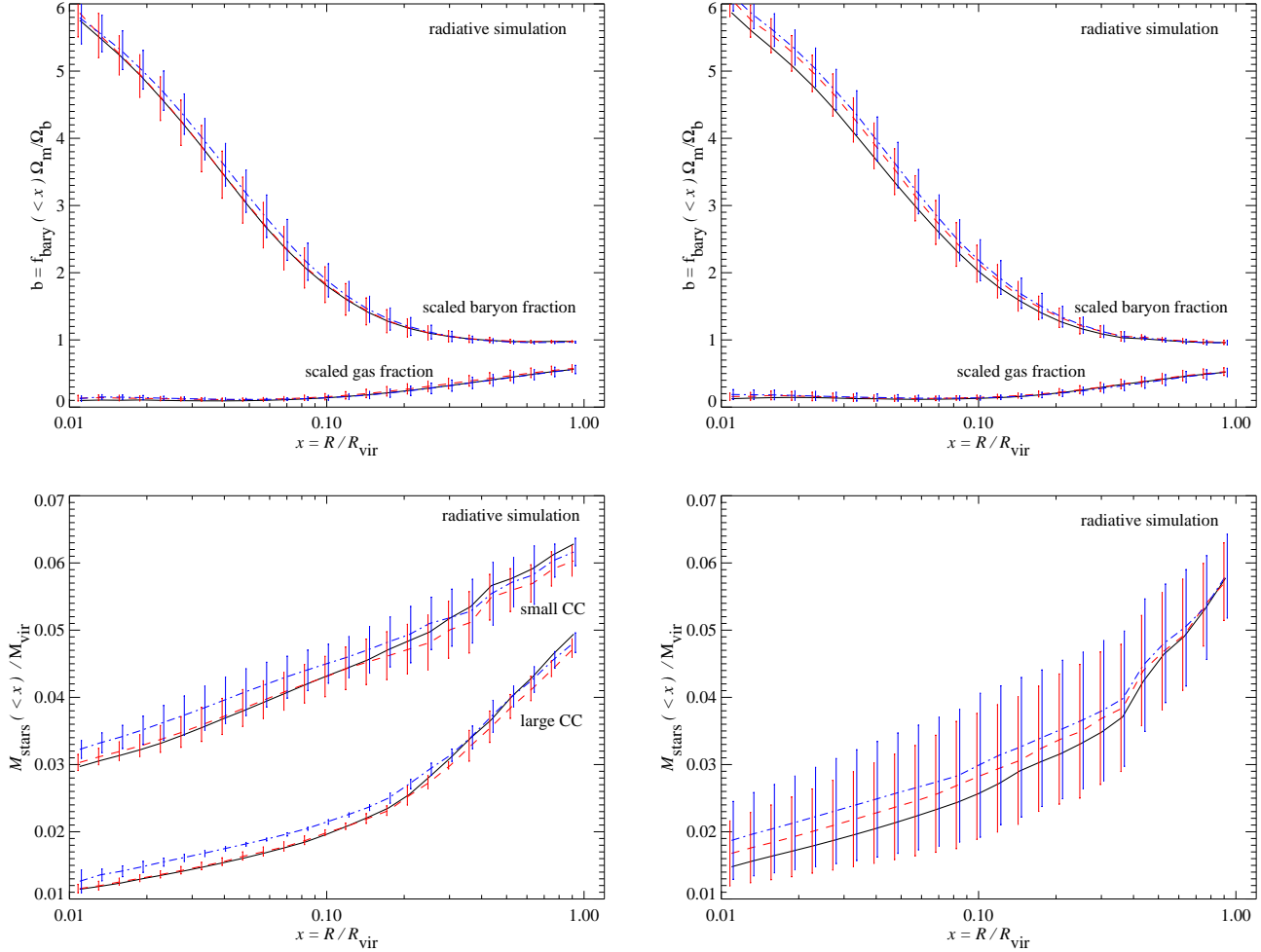*Cool core clusters:*   *Merging clusters:*

Figure 6. Average profiles of our sample of all cool core clusters (left-hand side) and merging clusters (right-hand side) in our radiative simulations at redshift $z = 0$. Shown are the appropriately scaled profiles of the thermal and CR pressure (P_{th} and P_{CR}, the latter with symbols), relative CR pressure $X_{CR} = P_{CR}/P_{th}$, and the effective adiabatic indices γ_{eff} (solid) in comparison with the CR adiabatic indices γ_{CR} (dashed). Colour scheme: black: reference simulations without CRs, red: CRs are injected only through shock acceleration using Mach number dependent scheme, blue: complete CR-model including CR injection from supernovae.

Figure 7. Average profiles of our sample of all cool core clusters (left-hand side) and merging clusters (right-hand side) in our radiative simulations at redshift $z = 0$. Shown are the appropriately scaled profiles of the baryon fraction b (top panels) and the stellar mass $M_{stars}(< x)$ (bottom panels). Colour scheme: black: reference simulations without CRs, red: CRs are injected only through shock acceleration using Mach number dependent scheme, blue: complete CR-model including CR injection from supernovae.

to the above mentioned over-cooling problem which has a higher relative impact in smaller systems. There are more stars formed in our complete CR model on scales $r < 0.3 R_{vir}$ irrespective of the dynamical state of the cluster while our CR-shock model shows less formed stellar mass in the outer cluster regions in our CC clusters. This shows again that the CR physics studied here aggravates the cooling flow problem in contemporary simulations.

3.3.7 Discussion of CRs profiles in radiative simulations

The CR distribution in the dilute outer cluster regions is dominated by the CR injection characteristics with its strong structure formation shocks that efficiently accelerate CRs into the IGM. The relative CR pressure X_{CR} decreases as we move inwards due to the same reasons that apply in the case of non-radiative simulations: (1) weak central flow shocks are inefficient in accelerating CRs, (2) adiabatic compression of a composite of CRs and thermal gas disfavours the CR pressure relative to the thermal pressure due to the

softer equation of state of CRs, and (3) CR loss processes are more important at the dense centres.

Rather than becoming dynamically unimportant as it is the case in our non-radiative simulations, the relative CR pressure increases strongly towards dense substructures if we consider radiative losses of the thermal gas due to the long CR cooling time scales compared to those of the thermal gas. The thermal gas cools much faster radiatively and diminishes its pressure support while it condenses out and forms stars. The high fraction of pressure support provided by CRs yields a higher compressibility of the composite fluid that requires a larger overdensity in order to balance the gravitational pressure from the dark matter and gas. This increases the density of each galactic substructure as well as in the cluster centre and leads to a pressure enhancement, provided the hydrostatic equation is applicable, $dP/(dr) = \rho_{gas} G M(< r) r^{-2}$. This higher density leads to a higher rate of star formation and thus increases the central baryon fraction since gas from larger scales has to replenish the condensed gas in order to maintain hydrostatic equilibrium.

In the case of ongoing merger activity, the relative CR pressure is boosted due to a combination of two effects: (1) a merger event triggers large random motions and merger shock waves that steepen considerably while they are running into the shallower cluster potential where they efficiently inject CRs. (2) These large random motions mix the highly CR-enriched intergalactic medium outside clusters with the ICM. Weak virialisation shocks traversing the cluster after the merger thermalize random gas motions, thus increase the thermal energy and yield a decrease of X_{CR}. CR loss processes and adiabatic compression furthermore decreases X_{CR} in intermediate cluster regions with a comparatively long thermal cooling time scale.

3.4 Cosmic ray related physical processes

In the following sections we study the physical processes related to CRs in more detail, which complements the previous sections. In particular, we will consider projected maps of physical cluster properties, and analyse the Mach number statistics during cluster formation. Finally, Sect. 3.5 studies the consequences of CRs for thermal observables such as X-ray emission and the Sunyaev-Zel'dovich effect.

3.4.1 Maps of physical quantities

We produced projected maps of the density, the mass-weighted temperature, CR related quantities, and thermal cluster observables. Generally, a three-dimensional scalar field $a(\mathbf{r})$ along any ray was calculated by distributing the product of $a(\mathbf{r})$ and the specific volume M_α/ρ_α of the gas particles over a grid comoving with the cosmic expansion. This yields the projected quantity $A(\mathbf{r}_\perp)$:

$$A(\mathbf{r}_{\perp,ij}) = \frac{1}{L_{pix}^2} \sum_\alpha a_\alpha \frac{M_\alpha}{\rho_\alpha} W_{\alpha,ij}(\mathbf{r}_{\perp,ij} - \mathbf{r}_\alpha), \qquad (4)$$

where $W_{\alpha,ij}$ is the value of the projected smoothing kernel (normalised to unity for the pixels covered) of an SPH particle α at comoving grid position $\mathbf{r}_{\perp,ij}$, and L_{pix}^2 is the comoving area of the pixel.

The surface mass density map was produced by projecting the quantity $a_\alpha = \rho_\alpha/(\Omega_b \rho_{cr})$ and the mass-weighted temperature map by setting $a_\alpha = T_\alpha \rho_\alpha$ divided by the mass projection. Figure 8 shows the radiative simulation of a super-cluster region (with the identifier g8) which is dominated by a large cool core cluster and surrounded by smaller satellite clusters. While the ICM of the central massive cluster reaches a temperature of the order of its virial temperature of $kT_{vir} = 13.1$ keV, the surrounding warm-hot intergalactic medium (WHIM) acquires temperatures of $kT \sim (10^{-2} - 10^{-1})$ keV. The spatial distribution of shock strengths can be studied best by looking at the Mach numbers weighted by the energy dissipation rate at shocks. The colour hue of the lower panel on the left-hand side of Fig. 8 has been chosen to represent the projected quantity $a_\alpha = \mathcal{M}_\alpha \dot{\varepsilon}_{diss,\alpha}$ divided by the projected energy dissipation rate $\langle \dot{\varepsilon}_{diss} \rangle_{los}$, where $\mathcal{M}_\alpha$ denotes the Mach number of the SPH particle. The brightness scales logarithmically with the projected dissipation rate $\langle \dot{\varepsilon}_{diss} \rangle_{los}$. Within this super-cluster region most of the energy is dissipated in weak internal shocks with Mach numbers $\mathcal{M} \lesssim 2$ which are predominantly central flow shocks or merger shock waves traversing the cluster centre. Collapsed cosmological structures are surrounded by several shells of external shocks with successively higher Mach numbers, but they play only a minor role in the energy balance of thermalization as can be inferred by its dim brightness. Clearly visible are spherical shells of

shocks at different radii from the cluster centre. Two distinct accretion shocks at distances of 2 and $3\,h^{-1}$ Mpc to the cluster centre are visible, followed by shells of stronger shocks further outwards.

Finally, the mass-weighted CR pressure relative to the total pressure $\tilde{X}_{CR} = P_{CR}/P_{tot}$ was obtained by projecting $a_\alpha = \rho_\alpha \tilde{X}_{CR,\alpha}$ divided by the mass projection (lower panel on the right-hand side of Fig. 8). The projections of the relative CR pressure support the picture inferred from our profiles. While $\tilde{X}_{CR}$ acquires comparatively high values within the WHIM that are hydrodynamically important, their importance diminishes (on average) within each galaxy cluster for reasons laid out above (cf. Sect. 3.3.7). Within each individual galaxy, the CR pressure reaches equipartition or dominates the thermal pressure as can be seen by the numerous yellow points sprinkled over the map, each corresponding to a galaxy. The time evolution of the relative CR pressure from $z = 1$ until today and the comparison of $\tilde{X}_{CR}$ for a large and a small CC cluster can be studied in more detail in Fig. 9, that shows the central regions of the galaxy cluster 1 and 10. At $z = 0$, the iso-contour of $\tilde{X}_{CR} = 0.1$ (the transition from green to red for our colour scale) roughly coincides with the virial radius in our small cluster $R_{vir} \simeq 0.7\,h^{-1}$ Mpc while it approximately lies at a scale of twice the virial radius in the large cluster ($R_{vir} \simeq 2\,h^{-1}$ Mpc). This already hints that weaker shocks are responsible for thermal dissipation in high mass halos compared to low mass halos. We will study this effect in more detail in the next section. The second striking observation is that at high redshifts the warmer colours dominate over the cooler ones, indicating a higher level of relative CR pressure at high redshift. This is because in the hierarchical model of structure formation, the characteristic halo mass and thus the associated characteristic temperature grow with cosmic time. The higher sound speeds of the diffuse gas at later times decreases the characteristic Mach numbers of the shocks responsible for thermalization and thus decreases the acceleration efficiency of CRs.

3.4.2 Mach number statistics

Earlier work on this subject (Miniati et al. 2000; Ryu et al. 2003; Pfrommer et al. 2006) classified structure formation shocks into two broad populations which are labelled as *internal* and *external* shocks. These categories have been distinguished on whether or not the associated pre-shock gas was previously shocked in the cosmic history. Since we are also interested in assessing the properties of shock waves in radiative simulations, it turns out to be favourable not to use a thermodynamical criterion such as the temperature but a criterion based on the overdensity $\delta_{gas} = \rho_{gas}/(\Omega_b \rho_{cr} a^{-3}) - 1$ in order not to confuse the shock definition in the presence of radiatively cooling gas in galaxies (here, ρ_{gas} denotes the physical gas mass density and a is the cosmic scale factor). In practice, we use the criterion of a critical pre-shock overdensity $\delta_{gas} > 10$ or the physical gas density $\rho_{gas} > 7.5 \times 10^{-24}$ g cm^{-3} for the classification of an internal shock. With this criterion, *external* shock surfaces surround filaments, sheets, and haloes where the pristine adiabatically cooling gas is shocked for the first time while *internal* shocks are located within the regions bound by external shocks and are created by flow motions accompanying hierarchical structure formation. Their population includes accretion shocks produced by infalling material along the filaments into clusters, merger shocks resulting from infalling haloes, and flow shocks inside nonlinear structures which are excited by supersonic motions of subclumps. The thermal gas of the warm-hot intergalactic medium has a low sound velocity $c = \sqrt{\gamma_{th} P/\rho} = \sqrt{\gamma_{th} kT/(\mu m_p)}$ owing to the low temperature, so once the diffuse gas breaks on mildly nonlinear
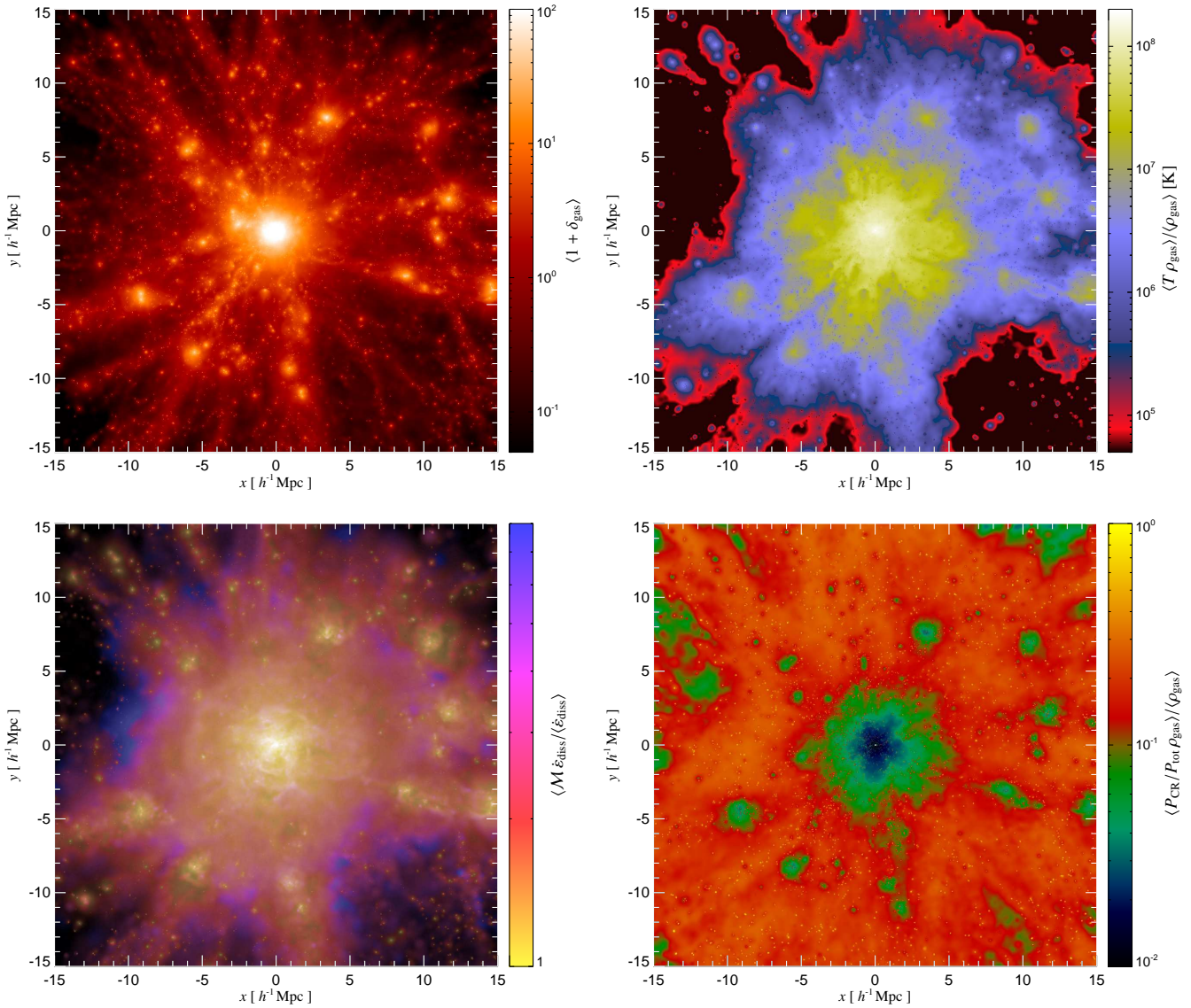
Figure 8. Environment of the largest galaxy cluster in our sample (a cool core cluster) in the radiative simulation including CRs from structure formation shocks only. Shown are the projected density, mass-weighted temperature, the Mach number of shocks weighted by the energy dissipation rate in colour (while the brightness displays the logarithm of the dissipation rate), and the mass weighted CR pressure relative to the total pressure. We performed line-of-sight averages to obtain the projected quantities.

structures, strong shock waves develop that are characterised by high Mach numbers $\mathcal{M} = v_s/c$. Nevertheless, the energy dissipation rate of internal shocks is always higher compared to external shocks within the WHIM because the mean shock speed and pre-shock gas densities are significantly larger for internal shocks.

To quantify these considerations, we compute the differential Mach number distribution weighted by the shock-dissipated energy $d^2 E_{diss}(a, \mathcal{M})/(d \log a \, d \log \mathcal{M})$ at different redshifts characterised by scale factor a. The top left-hand panel of Fig. 10 shows this Mach number distribution in our non-radiative simulation of a super-cluster region (g8), while the top right-hand panel shows this distribution for the radiative simulation using the same initial conditions. The lower left-hand panel shows both distributions integrated over the scale factor, $d E_{diss}(\mathcal{M})/(d \log \mathcal{M})$. Internal shocks are shown with dotted lines and external shocks with dashed lines.

The lower right-hand panel shows again the integrated Mach number distribution. This time, however, the shock population is subdivided into two categories that are separated by the overdensity threshold $\delta_{gas} > 10^4$ to study the origin of the flat horizontal tail of the Mach number distribution extending to very high Mach numbers in our simulation with radiative gas physics.

Several important points are apparent. (1) The non-radiative simulation shows a smooth distribution that is skewed towards lower values of the Mach number. The mean of the Mach number distribution weighted by the dissipated energy decreases as cosmic time evolves, i.e. the average shock becomes weaker at later times. (2) In contrast, the radiative simulation shows a broad symmetric distribution in $\log \mathcal{M}$ at early times and develops later on a peak at low Mach numbers that resembles that in the non-radiative case followed by a significant disturbed tail towards higher Mach num-
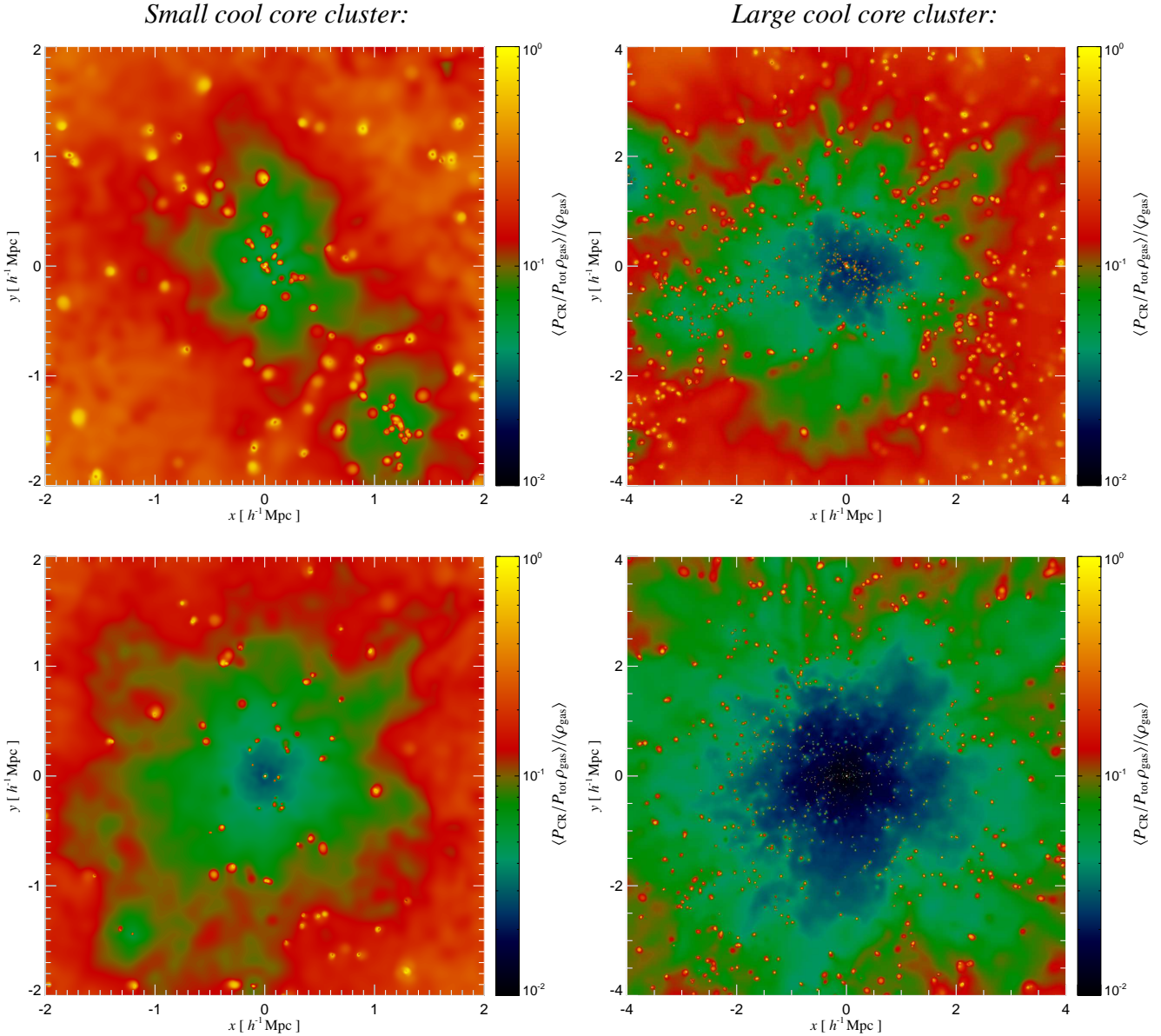
Small cool core cluster: *Large cool core cluster:*

Figure 9. Time evolution of the mass-weighted CR pressure relative to the total pressure in the radiative simulation including CRs from structure formation shocks. Upper panels show the clusters at $z = 1$, the lower panels at $z = 0$. Left panels: small cool core cluster with a virial mass of $8.8 \times 10^{13}\, h^{-1}\, \mathrm{M_\odot}$ at $z = 0$. Right panels: large cool core cluster with a virial mass of $1.8 \times 10^{15}\, h^{-1}\, \mathrm{M_\odot}$.

bers of $\mathcal{M} \gtrsim 10$. Due to this tail, the mean of the distribution is not a monotonic function of time any more and achieves high values of $\langle \mathcal{M}\, \mathrm{d}\dot{E}_{\mathrm{diss}}/(\mathrm{d}\log\mathcal{M})\rangle / \langle \mathrm{d}\dot{E}_{\mathrm{diss}}/(\mathrm{d}\log\mathcal{M})\rangle \simeq 100$ already at $z = 10$. This reflects the merging history of the clusters forming in that simulation in combination with the ongoing development of dense cooling regions that permit the formation of strong shocks during merger events. (3) The time integrated Mach number distribution weighted by the dissipated energy, $\mathrm{d}E_{\mathrm{diss}}(\mathcal{M})/(\mathrm{d}\log\mathcal{M})$, peaks at Mach numbers $\mathcal{M} \lesssim 2$. Compared to full-size cosmological simulations, the peak position remains unchanged while the smooth tail in our non-radiative super-cluster simulation is shifted towards lower values (cf. Pfrommer et al. 2006, Fig. 6). In non-radiative simulations, the peak of the Mach number distribution originates from weak flow shocks internal to dense halo regions, while the smooth tail towards strong shocks results from external shocks

where the diffuse gas breaks on mildly nonlinear structures. These under-dense regions are under-represented in our super-cluster simulation and thus we miss a subsample of this shock population compared to the cosmic mean. (4) The horizontal tail extending towards high Mach numbers in radiative simulations can unambiguously be attributed to internal shocks within cooled high-density regions of $\delta_{\mathrm{gas}} > 10^4$. Part of this result is due to the over-cooling of these dense regions in our radiative simulation, which yields an over-estimate of the Mach numbers due to the too small sound speeds. However, the main contribution in terms of energy dissipation originates from internal shocks that occur in regions with a pre-shock overdensity $10 < \delta_{\mathrm{gas}} < 10^4$. This is because most of the ICM that is being virialised lies simply at overdensities $\delta_{\mathrm{gas}} < 10^4$. (5) In both types of simulations, there is an increasing amount of energy dissipated at shock waves per logarithmic interval in the scale factor as
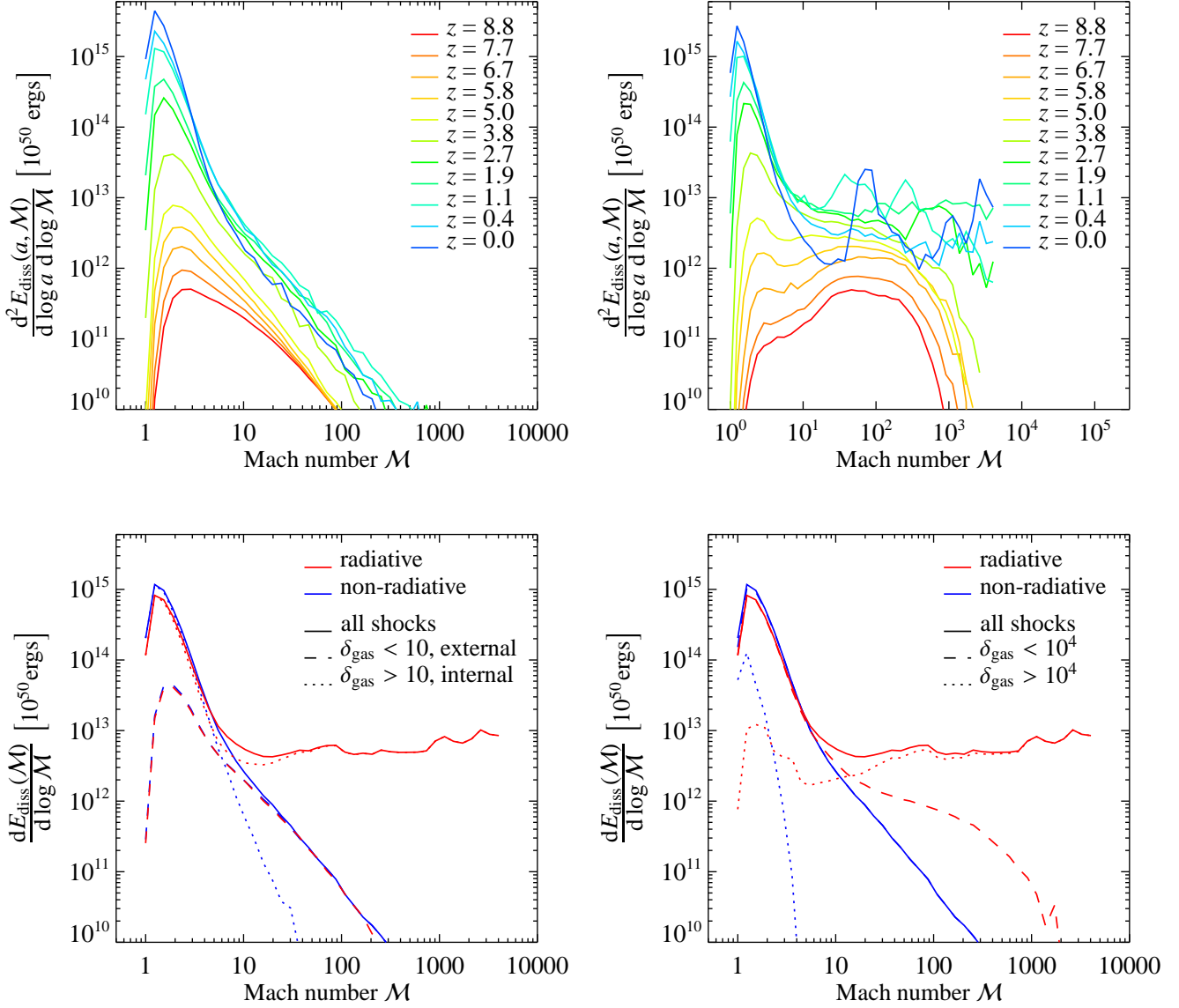
Figure 10. Influence of radiative cooling and star formation on the Mach number statistics of high-resolution cluster simulations (g8). The *top left-hand panel* shows the differential Mach number distribution $d^2 E_{\mathrm{diss}}(a, \mathcal{M})/(d \log a \, d \log \mathcal{M})$ for our non-radiative simulation while the *top right-hand panel* shows this distribution for the radiative simulation. The *lower left-hand panel* shows both distributions integrated over the scale factor, $dE_{\mathrm{diss}}(\mathcal{M})/(d \log \mathcal{M})$. External shocks (occurring in overdensities $\delta_{\mathrm{gas}} = \rho_{\mathrm{gas}}/(\Omega_{\mathrm{b}} \, \rho_{\mathrm{cr}} \, a^{-3}) - 1 < 10$) are shown with dashed lines and internal shocks ($\delta_{\mathrm{gas}} > 10$) with dotted lines. The *lower right-hand panel* shows again the integrated Mach number distribution, $dE_{\mathrm{diss}}(\mathcal{M})/(d \log \mathcal{M})$. Here, the shock populations are subdivided into two categories that are separated by the overdensity threshold $\delta_{\mathrm{gas}} = 10^4$. This shows unambiguously that the flat tail of the Mach number distribution in radiative simulations originates from internal shocks within cooled high-density regions that are almost absent in non-radiative simulations.

the universe evolves because the mean shock speed is significantly growing when the characteristic mass becomes larger with time. This trend starts to level off at redshift $z \simeq 1$ when galaxy clusters are in place.

Figure 11 compares the shock strengths of our super-cluster region (g8) with that of an isolated small cluster region (g676). While the dissipated energy integrated over the cosmic formation history in our simulation of the isolated small cluster (g676) amounts to $E_{\mathrm{diss}} = 2.4 \times 10^{62}$ erg, in our large super-cluster simulation (g8) the amount of dissipated energy was two orders of mag-

nitude larger, $E_{\mathrm{diss}} = 2.4 \times 10^{64}$ erg. Normalising the Mach number distribution $dE_{\mathrm{diss}}(\mathcal{M})/(d \log \mathcal{M})$ with E_{diss}, we observe in our radiative as well as in our non-radiative simulation that the characteristic Mach number which is responsible for the energy dissipation decreases with cluster mass due to the increasing sound speed in more massive systems. In other words, weaker shocks are responsible for the energy dissipation in larger systems. Apparently, the characteristic shock speed in these large systems does not increase accordingly to make up for the increase in sound speed. This confirms the suggestion of Jubelgas et al. (2006) that virialisation pro-
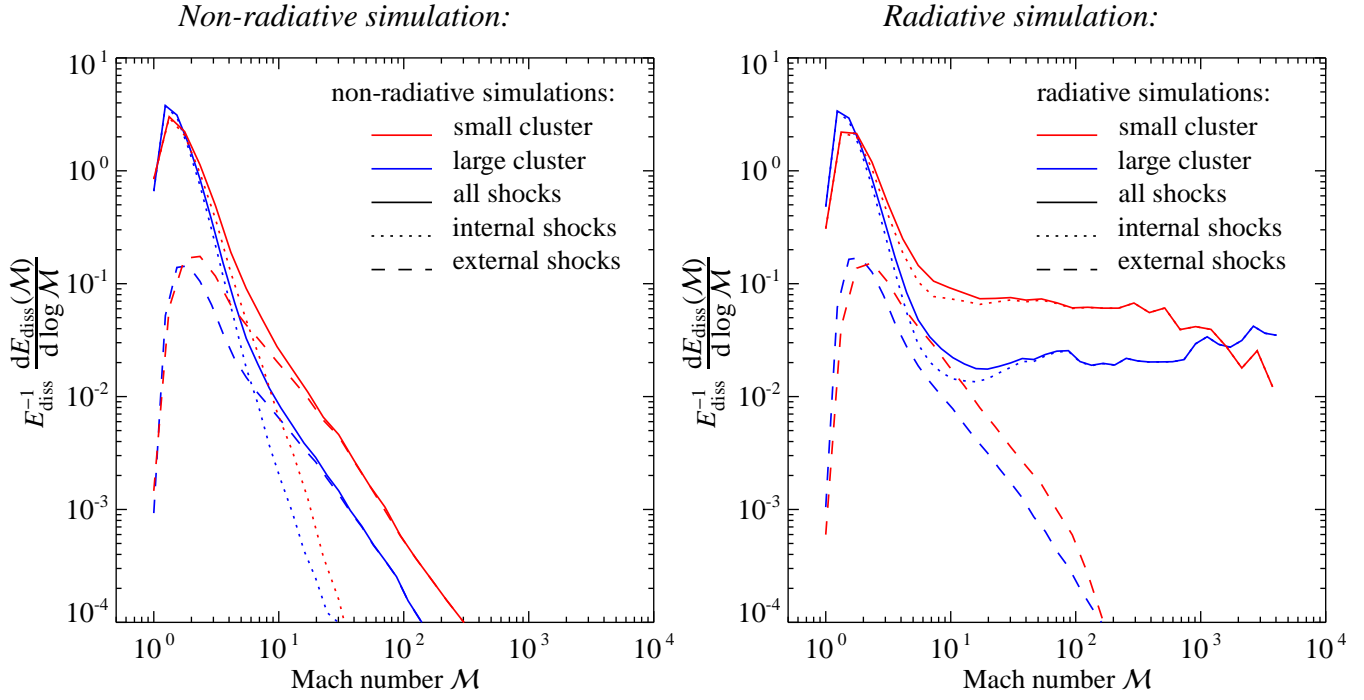
Figure 11. Influence of the cluster size on the Mach number statistics of high-resolution cluster simulations. The *left-hand panel* compares the appropriately scaled Mach number distribution $dE_{diss}(\mathcal{M})/(d\log\mathcal{M})$ of a large super-cluster region (g8) and a small isolated cluster region (g676) in our non-radiative simulation, while the *right-hand panel* shows the comparison in our simulation with radiative gas physics. Internal shocks (occurring at overdensities $\delta_{gas} = \rho_{gas}/(\Omega_b \rho_{cr} a^{-3}) > 10$) are shown with dotted lines and external shocks with dashed lines. The total dissipated energy integrated over the cosmic formation history in our simulation of our isolated small cluster (g676) amounts to $E_{diss} = 2.4 \times 10^{62}$ erg, in our large super-cluster simulation (g8) the amount of dissipated energy was two orders of magnitude larger, $E_{diss} = 2.4 \times 10^{64}$ erg. The characteristic Mach number which is responsible for the energy dissipation decreases with cluster mass due to the increasing sound speed in those systems.
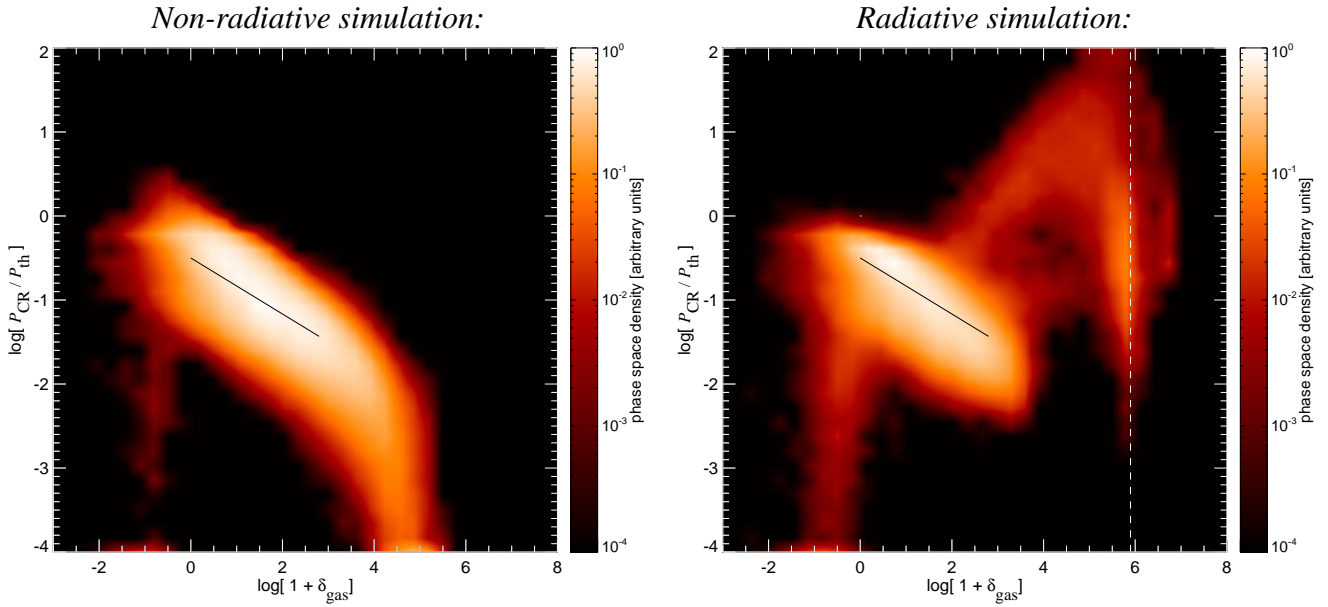

Figure 12. Phase space distribution of the CR pressure relative to the thermal pressure at $z = 0$. Left-hand side: radiative simulation, right-hand side: non-radiative simulation of our small cluster 10. The black line shows a track of constant entropy of a composite of CRs and thermal gas during adiabatic compression (using the same normalisation in both panels to guide the eye). Dashed white line: star formation threshold of the simulation. Shown is the distribution of SPH particles with $r < 10 R_{vir}$ that are identified by being in regions not contaminated by boundary dark matter particles in the simulation of cluster 10.
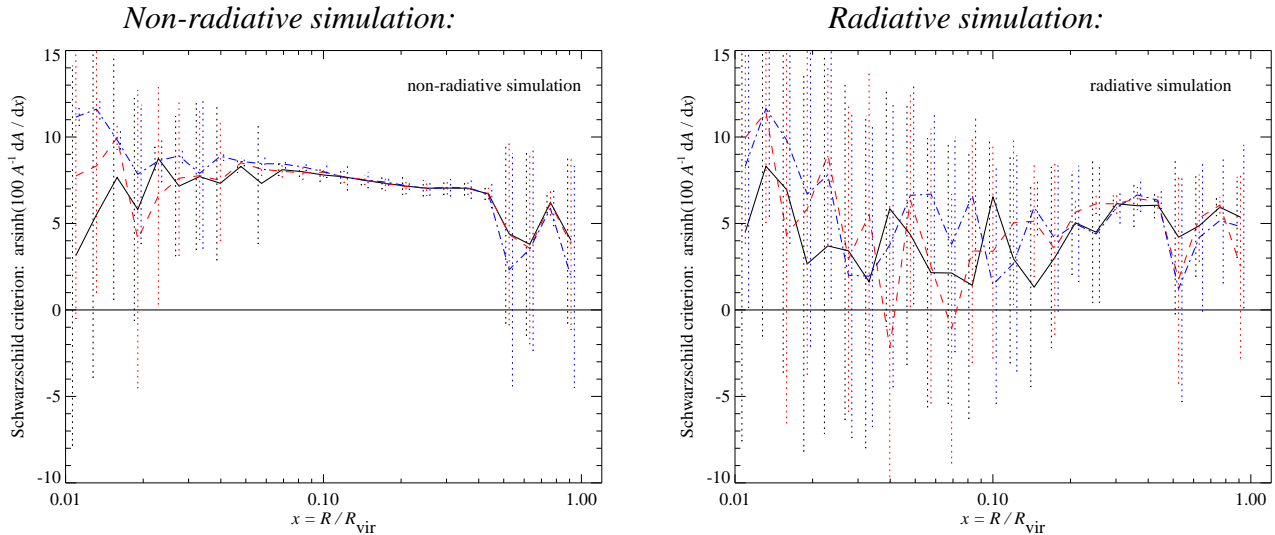
Figure 13. Average profiles of the Schwarzschild criterion for convective instability of all clusters. Left-hand side: non-radiative simulations, right-hand side: radiative simulations. Positive values of this criterion indicate convective stability. Colour scheme: black: reference simulations without CRs, red: CR are injected only through shock acceleration using Mach number dependent scheme, blue radiative: full model including CRs from supernovae, blue non-radiative: CR shock acceleration with constant energy injection efficiency.

cesses in more massive systems is mediated by shocks with smaller Mach numbers. Since strong shocks are more effective in accelerating CRs, the relative CR pressure level is increased in low mass halos as shown in Table 3 and Fig. 9.

3.4.3 *Cosmic ray phase space distributions*

Figure 12 compares the phase space distribution of the CR population at $z = 0$ of a radiative simulation to a non-radiative simulation. Specifically, we present the CR pressure relative to the thermal pressure, X_{CR}, versus the overdensity of the gas $\delta_{gas} + 1 = \rho_{gas}/(\Omega_b \rho_{cr} a^{-3})$. Thus, this figure shows the variance in X_{CR} at a given overdensity δ_{gas} in our simulations of cluster 10. At low densities, both phase space distributions resemble each other. Low density regions are characterised by strong shocks that efficiently accelerate CRs and yield a high value of X_{CR}. As we move inwards the cluster, the density increases and the characteristic shock strength decreases which makes CR acceleration less efficient; an effect that reduces X_{CR}. Adiabatic compression of a composite of CRs and thermal gas disfavours the CR pressure relative to the thermal pressure due to the softer equation of state of CRs. This is visualised by the black line which shows a track of constant entropy $X_{CR} \propto \delta_{gas}^{\gamma_{CR} - \gamma_{th}}$ of a composite of CRs and thermal gas during adiabatic compression. Finally, CR loss processes are more important in denser regions, a third process that reduces X_{CR}. While the story ends here for the non-radiative simulations, it goes an important step beyond in radiative simulations. There, the thermal gas cools on a small timescale, diminishes pressure support, condenses out of the gaseous phase and eventually forms stars at the characteristic density threshold as indicated by the white dashed line. Meanwhile, the relative CR pressure increases due to the comparatively long CR cooling time leading to a CR pressure that dominates over the thermal one at densities $\delta_{gas} > 10^4$. Finally, at the star formation threshold, we obtain a very broad distribution of X_{CR}.

3.4.4 *CR buoyancy – the generalised Schwarzschild criterion*

Figure 13 shows the generalised Schwarzschild criterion for convective instability of our sample of all clusters. The criterion for convective stability is given by

$$\frac{\Delta \ln A}{\Delta r} > 0, \tag{5}$$

where the effective entropic function is denoted $A = (P_{th} + P_{CR})\rho^{-\gamma_{eff}}$ (cf. Eqn. (A8)). The ICM of our non-radiative and radiative simulations is overall convectively stable. This is no surprise since in any convective unstable region, the dynamics of the instability will quickly restore a stable configuration, thus instabilities are self-erasing. The radiative simulations show a larger cluster-to-cluster variation with respect to individual radial bins, preferably in merging clusters that are formally convectively unstable. Infalling clumps of matter distort the spherically averaged profile such that the Schwarzschild criterion classifies them as convectively unstable. The simulations including CR physics do not show significantly different behaviour compared to our reference simulations. CRs from supernovae shocks that are injected near the cluster centre could have triggered convective instabilities as proposed by Chandran (2004), but this is not really seen in our simulations. The situation might be different and more unstable if one included an additional central source in the form of CRs that are diffusing out of AGN bubbles at cluster centres.

3.5 Thermal cluster observables

3.5.1 *Enhanced X-ray emission*

Our map of the bolometric X-ray surface brightness in the bremsstrahlung regime was produced by means of Eqn. (4), projecting the quantity

$$a_\alpha = \Lambda_0 \left(\frac{kT_\alpha}{keV}\right)^{1/2} \left(\frac{\rho_\alpha}{\mu m_p}\right)^2, \tag{6}$$

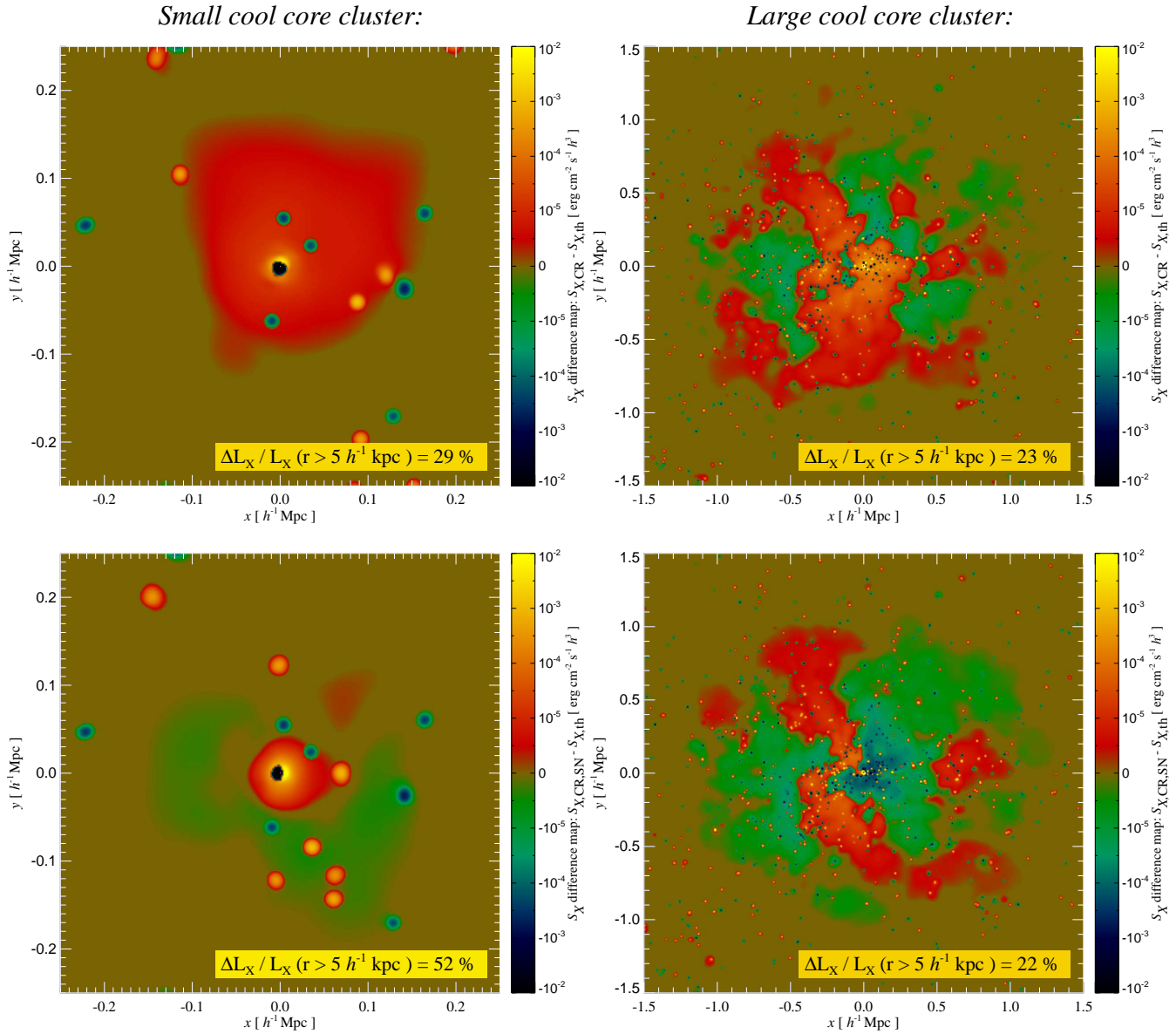*Small cool core cluster:*   *Large cool core cluster:*

Figure 14. Difference of the X-ray surface brightness in a radiative simulation with CRs and the corresponding reference simulation without CRs. Left-hand side: small cool core cluster with a virial mass of $8.8 \times 10^{13} \, h^{-1}$ Mpc at $z = 0$, right-hand side: large cool core cluster with a virial mass of $1.8 \times 10^{15} \, h^{-1}$ Mpc. Upper panels: simulations only account for CR acceleration at structure formation shocks, lower panels: CRs from supernovae are also considered. The relative difference of the integrated X-ray luminosity (excluding the central over-cooling region of $r < 5 \, h^{-1}$ kpc) is given in the inlay.

$$\Lambda_0 = \left(\frac{2\pi \, \text{keV}}{3 \, m_\text{e}} \right)^{1/2} \frac{2^5 \, \pi \, e^6}{3 \, h \, m_\text{e} c^3} \bar{g}_\text{B}(T_\alpha) \mu^2 \frac{1 + X_\text{H}}{2} \tag{7}$$

$$= 1.78 \times 10^{-24} \, \text{erg cm}^{-3} \, \text{s}^{-1}. \tag{8}$$

Here, T_α denotes the temperature of the SPH particle (labelled with α), h denotes the Planck constant, e the elementary charge, $X_\text{H} = 0.76$ is the primordial hydrogen mass fraction, $\mu = 4/(5X_\text{H} + 3) = 0.588$ is the mean molecular weight of fully ionised gas, and $\bar{g}_\text{B} \simeq 1.2$ is the frequency- and velocity-averaged Gaunt factor (Rybicki & Lightman 1979; Spitzer 1978). To be self-consistent within the bremsstrahlung assumption, we assume a fully ionised gas of primordial element composition which consists of hydrogen and helium only.

Figure 14 shows the difference of the X-ray surface brightness

in a radiative simulation with CRs and the corresponding reference simulation without CRs. The small blue and yellow circles represent individual galaxies in each of the simulations whose orbits did not match up when one includes different physical CR processes such that small changes in the energy budget modify the galactic orbits, accumulate and eventually lead to macroscopic separation of equivalent galaxies in the final spatial distribution. The left-hand side shows a small cool core cluster with a virial mass today of $8.8 \times 10^{13} \, h^{-1}$ Mpc (cluster 10) and the right-hand side a large cool core cluster with a virial mass today of $1.8 \times 10^{15} \, h^{-1}$ Mpc (cluster 1). While the upper panels show the simulation that only accounts for CR acceleration at structure formation shocks, the simulations displayed in the lower panels take also CRs from supernovae into account. The relative difference of the integrated X-ray lumi-

Table 4. : CR   X-   C   -y

Cl.	sim.'s	dyn. state[1]	$T_{200}^{[1]}$ [keV]	$\Delta L_X/L_X^{[2]}$ shock-CRs[3]	$\Delta L_X/L_X^{[2]}$ compl. CRs[3]	$\Delta Y/Y$ shock-CRs[3]	$\Delta Y/Y$ compl. CRs[3]	$\Delta y_0/y_0$ shock-CRs[3]	$\Delta y_0/y_0$ compl. CRs[3]	y_0 $[10^{-5}]$
1	g8a	CC	13.1	+23%	+22%	+0.1%	−0.6%	+ 8%	± 0%	26.7
2	g1a	CC	10.6	+18%	+14%	+1.1%	−0.1%	+ 8%	− 4%	15.4
3	g72a	PostM	9.4	+ 9%	+15%	−1.6%	−0.1%	− 7%	− 7%	14.6
5	g1b	M	4.7	+16%	+69%	−1.5%	+1.1%	+ 7%	− 4%	2.73
9	g1d	M	1.7	−10%	+ 8%	−4.5%	−2.2%	−12%	− 1%	0.475
10	g676	CC	1.7	+29%	+52%	−0.8%	−4.5%	+23%	+41%	0.960
11	g914	CC	1.6	+36%	+23%	−0.1%	−3.7%	+25%	+ 5%	1.01

N :
(1) The definitions for the dynamical state of the cluster and the virial temperature is given in Table 2.
(2) The relative difference of the integrated X-ray luminosity has been computed without taking into account the central over-cooling region of $r < 5\,h^{-1}$ kpc. Positive values for the relative difference indicate an enhancement of the thermal cluster observable when taking CRs into account.
(3) The shock-CR model is represented by our radiative simulations that account only for structure formation CRs while the complete model is based on our radiative simulations that take additionally supernova CRs into account.

nosity (without the central over-cooling region of $r < 5\,h^{-1}$ kpc) is given in the inlay, appropriately colour-coded such that the integrated CR effect on the X-ray luminosity can be easily read off from the colour bar. All these simulations show an enhancement of the central and integrated X-ray luminosity in our CR models compared to our reference models without CRs. This effect derives from the softer effective adiabatic index in the CR simulations due to the large ratio of the CR-to-thermal cooling time in the cluster centre, leading to a more compressible gas with an associated density increase that is required to balance the gravitational pressure of the dark matter. The resulting enhancement of the X-ray surface brightness is more pronounced in small CC clusters due to the higher level of relative CR pressure in combination with a relaxed spherically symmetric structure.

Our previous considerations are confirmed by analysing a representative subsample of our cluster simulations with respect to mass and dynamical state in Table 4. Positive values for the relative difference indicate an enhancement of the thermal cluster observable when taking CRs into account. While the differences of the cool core cluster simulations yield a consistent picture in our runs which account for CRs from structure formation shocks only, the sign and the magnitude of the CR-induced effects in merging systems do not follow a uniform trend due to the merger induced inhomogeneities in the ICM. In our complete CR model, the cluster-to-cluster variation of the CR enhancement of equally sized clusters is larger due the CR injection by supernovae, which traces the current star formation rate rather than being an integrated measure over the past cluster/core activity like in our CR-shock runs.

We can get a quantitative idea of the approximate size of this CR effect by employing a toy model of cluster formation in the presence of a CR component which we compare to a model without CRs. Consider at some early stage around $z \sim 2-3$ a composite of thermal gas and CRs that has been shock heated for the first time while it was collapsing into mildly non-linear structures. Today's analogue for such a state of the gas might be given by the WHIM which is characterised by a comparatively high relative CR pressure contribution of roughly $X_{CR} \sim 0.3 - 0.5$. Let us assume that the initial thermal pressure in our reference model without CRs is equivalent to the initial total pressure in our composite model with CRs, $P_{th,0}^* = P_{th,0} + P_{CR,0} = P_{th,0}(1 + X_{CR,0})$, where our reference quantities are denoted by a star. Neglecting radiative cooling and CR diffusion for simplicity, further accretion of new shells of mass

onto the dark matter halo exerts a pressure that adiabatically compresses the gas internal to the halo, yielding

$$P_{th} = P_{th,0}\, C^{\gamma_{th}} \qquad \text{and} \qquad P_{CR} = P_{CR,0}\, C^{\gamma_{CR}}. \qquad (9)$$

While the gas in our reference model is compressed by the factor C^*, the compression factor in the CR model is given by C. Requiring that the final pressure after adiabatic compression in both models is equivalent to each other, we obtain the condition

$$\left(\frac{C}{C^*}\right)^{\gamma_{th}} + X_{CR,0}\left(\frac{C}{C^*}\right)^{\gamma_{CR}} C^{*\,\gamma_{CR}-\gamma_{th}} - (1 + X_{CR,0}) = 0. \qquad (10)$$

This equation can be solved for the combination C/C^*. Assuming an initial relative CR pressure of $X_{CR,0} \simeq 0.3$, a compression factor in the reference model of $C^* \simeq 10^3$, and equivalent initial densities in both models, we obtain a density enhancement for our toy cluster in our CR model of $\Delta\rho/\rho^* \simeq 15$ per cent relative to the reference model. The associated X-ray emission would be enhanced in the presence of CRs by a factor of $\Delta L_X/L_X^* \simeq 32$ per cent compared to the model without CRs. This result should be taken with a grain of salt since we did not consider shock heating, radiative cooling, nor any CR transport and loss processes. It merely illustrates the important effect of the softer equation of state of CRs.

3.5.2 Modified Sunyaev-Zel'dovich effect

The amplitude of the thermal Sunyaev-Zel'dovich effect is given by the Compton-y parameter and is proportional to the line-of-sight integral of the thermal pressure which is obtained by replacing α in Eqn. (4) by

$$a_\alpha = \frac{\sigma_T}{m_e c^2}\,(\gamma_{th} - 1)\, X_H\, x_{e,\alpha}\, \mu\, u_\alpha\, \rho_\alpha, \qquad (11)$$

where $X_H = 0.76$ is the primordial hydrogen mass fraction, $x_{e,\alpha}$ is the ratio of electron and hydrogen number densities of the SPH particle (labelled with α) which we dynamically track in our radiative simulations, $\mu = 4/(3X_H + 1 + 4 X_H x_{e,\alpha})$ denotes the mean molecular weight of partly ionised gas, u_α is the internal energy per unit mass, and ρ_α is the physical mass density of the SPH particle.

Figure 15 shows the difference between the Compton-y parameter in a radiative simulation with CRs and the corresponding reference simulation without CRs. The left-hand side shows a small cool core cluster with a virial mass today of $8.8 \times 10^{13}\,h^{-1}$ Mpc
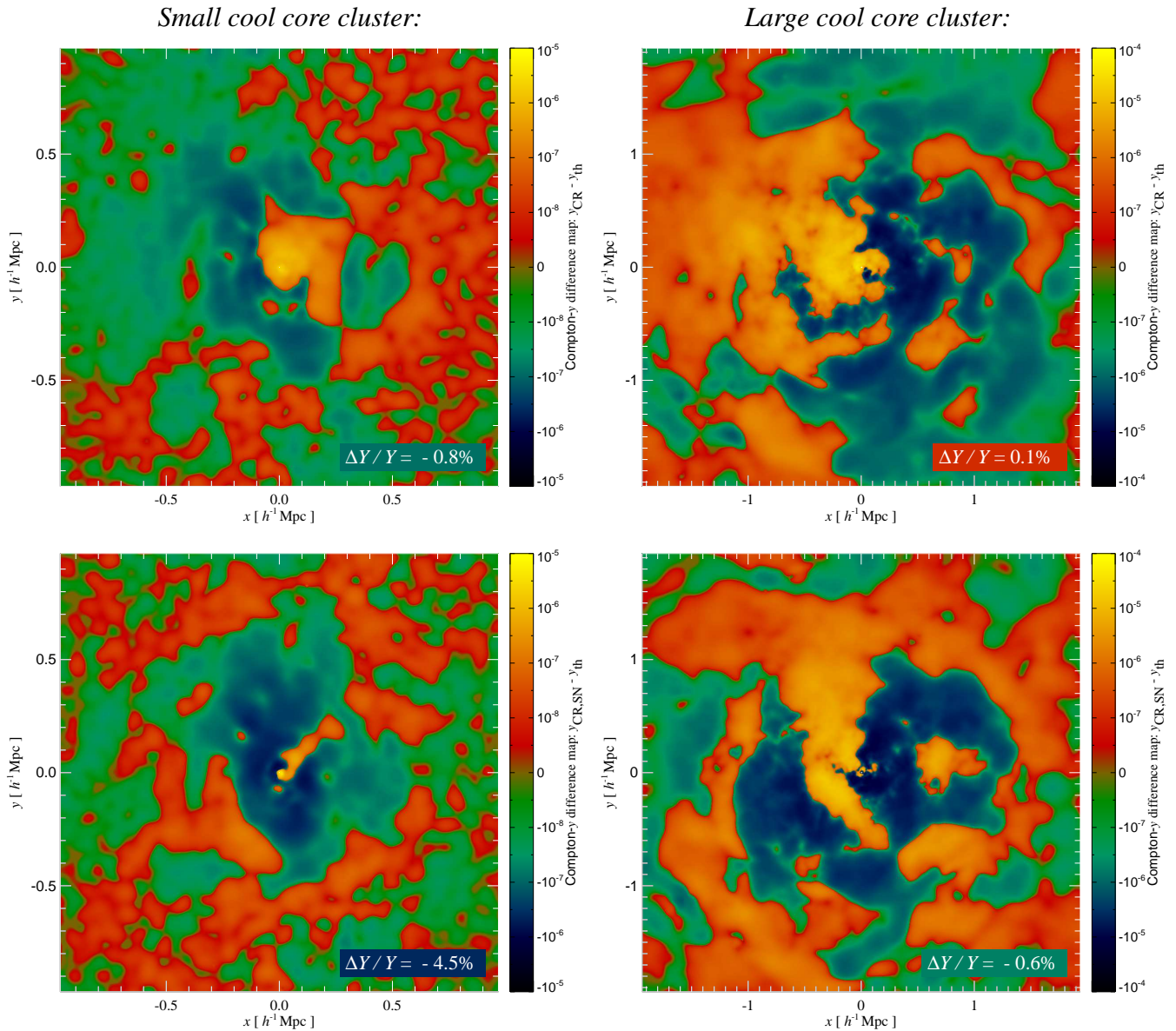
Figure 15. Difference of the Compton-y parameter in a radiative simulation with CRs and the corresponding reference simulation without CRs. Left-hand side: small cool core cluster with a virial mass of $8.8 \times 10^{13}\, h^{-1}$ Mpc at $z = 0$, right-hand side: large cool core cluster with a virial mass of $1.8 \times 10^{15}\, h^{-1}$ Mpc. Upper panels: simulations only account for CR acceleration at structure formation shocks, lower panels: additionally, CRs are also injected by supernova shocks. The relative difference of the integrated Compton-y parameter is given in the inlay.

(cluster 10) and the right-hand side displays a large cool cluster with a virial mass today of $1.8 \times 10^{15}\, h^{-1}$ Mpc (cluster 1). While the upper panels show the simulations that only account for CR acceleration at structure formation shocks, the simulations displayed in the lower panels take also CRs from supernovae into account. The relative difference of the integrated Compton-y parameter is given in the inlay, appropriately colour-coded such that the CR effect on the integrated Compton-y parameter can easily be read off from the colour bar. In the small cluster simulation, CR feedback leads to an enhancement of the central Compton-y parameter followed by a ring of a (much weaker) decrement. The more massive system shows a more asymmetric difference map with a larger contrast at the centre that is roughly one order of magnitude larger compared to the smaller system, as expected for the larger virial

mass. As analysed in Sect. 3.3, the high fraction of pressure support provided by CRs in the central regions results in a higher compressibility of the composite fluid, which in turn requires a larger overdensity in order to balance the gravitational pressure from the dark matter and gas. This increases the central density of the cluster and leads to a pressure enhancement, provided the hydrostatic equation is applicable, $\mathrm{d}P/(\mathrm{d}r) = \rho_{\mathrm{gas}}\, G\, M(<r)\, r^{-2}$. Hence, the Compton-$y$ parameter in our CR simulations shows a profile that is more peaked compared to our reference case. The increased central Compton-y parameter comprises a larger area in our CR-shock model compared to the complete CR model. This is due to the additional CR injection from SN in our complete CR model that reduces the amount of thermal SN feedback and thus reduces the Compton-y parameter.

Table 4 confirms this finding in a representative cross section of our clusters by showing the central Compton-y parameter y_0 as well as the relative difference of y_0. In practice, this quantity will be smoothed by the experimental beam which we did not try to model here. The behaviour of $\Delta y_0/y_0$ is much more regular in our shock-CR model since the CR effects are integrated over a longer timescale. In contrast, there is a larger variation of $\Delta y_0/y_0$ in our complete CR model, even among nearly similarly evolving clusters (cluster 10 and cluster 11), due to the central CR injection by supernovae which reflects the current central star formation rate.

The total Compton-y parameter Y of a galaxy cluster is given by the Compton-y parameter integrated over the solid angle element subtended by the cluster,

$$Y = D_{\mathrm{ang}}^2 \int_{\Omega_{\mathrm{cluster}}} \mathrm{d}\Omega\, y(\boldsymbol{\theta}) = \int_{A_{\mathrm{cluster}}} \mathrm{d}^2 x\, y(\boldsymbol{x}_\perp) = \frac{\sigma_{\mathrm{T}}}{\gamma_{\mathrm{th}} - 1} \frac{E_{\mathrm{th}}}{m_{\mathrm{e}} c^2}, \quad (12)$$

where D_{ang} is the angular diameter distance to the cluster. Interestingly, the total Compton-y parameter seems to be robust with respect to CR feedback because it reflects the cluster's total thermal energy E_{th}. We confirm this finding by looking at a representative cross section of clusters in our sample in Table 4. In large CC clusters, CR feedback has a negligible effect on the total Compton-y while in merging clusters, the total Compton-y parameter can either be slightly enhanced or decreased, depending on the merger virialisation progress of the induced shock waves leading to temporary inhomogeneities in the ICM. In small CC clusters, the value of Y is only slightly decreased in our CR-shock model while this effect is more pronounced in our complete CR model where Y is systematically decreased by 4 per cent due to the additional CR injection from SN that reduces the Compton-y parameter.

4 SUMMARY

We performed high-resolution simulations of a sample of 14 galaxy clusters that span a mass range from $5 \times 10^{13} h^{-1}\,\mathrm{M}_\odot$ to $2 \times 10^{15} h^{-1}\,\mathrm{M}_\odot$ to study the effects of cosmic rays (CRs) on thermal cluster observables such as X-ray emission and the Sunyaev-Zel'dovich effect. In a systematic study, we analyse the CR effects on the intra-cluster medium while simultaneously taking into account the cluster's dynamical state as well as the mass of the cluster. The modelling of the cosmic ray physics includes adiabatic CR transport processes such as compression and rarefaction, and a number of physical source and sink terms which modify the cosmic ray pressure of each particle. The most important sources considered are injection by supernovae (in our radiative simulations) and diffusive shock acceleration at cosmological structure formation shocks, while the primary sinks are thermalization by Coulomb interactions, and catastrophic losses by hadronic interactions. While the relative pressure contained in CRs within the virial radius is of the order of 2 per cent averaged over our cluster sample in non-radiative simulations, their average contribution rises to 32 per cent in our simulations with dissipative gas physics including radiative cooling, star formation, and supernova feedback.

Our main findings for the CR pressure relative to the thermal pressure $X_{\mathrm{CR}} = P_{\mathrm{CR}}/P_{\mathrm{th}}$ can be summarised as follows. The CR distribution in the dilute outskirts of cluster is dominated by the effective CR acceleration at strong structure formation shocks such as accretion and merger shocks. The relative CR pressure X_{CR} decreases as we move inwards to smaller cluster radii that are characterised by an increase of the sound speed and the density of the intracluster medium (ICM): (1) weak central flow shocks are ineffi-

cient in accelerating CRs, (2) adiabatic compression of a composite of CRs and thermal gas disfavours the CR pressure relative to the thermal pressure due to the softer equation of state of CRs, and (3) CR loss processes are more important at the dense centres.

Interestingly, if we include radiative losses of the thermal gas, the relative CR pressure increases strongly towards the cluster centre and inside dense galactic substructures within the ICM, because of the long CR cooling times compared to those of the thermal gas in these cooling environments. The thermal gas cools much faster radiatively and diminishes its pressure support while it condenses out and forms stars that do not participate in the pressure balance. In contrast, at a fixed density, the CR cooling time of an aged CR population remains almost constant as the thermal gas is cooling. High fraction of pressure support provided by CRs yields a higher compressibility of the composite fluid that requires a larger overdensity in order to balance the gravitational pressure from the dark matter and gas. This increases the density of each galactic substructure as well as in the cluster centre where it leads to a pressure enhancement, provided the hydrostatic equation is applicable as it is the case in cool core clusters. This higher density leads to a higher rate of star formation and thus increases the central baryon fraction strongly because gas from larger scales has to replenish the condensed gas in order to maintain hydrostatic equilibrium. We note that in real galaxy clusters this effect is expected to be somewhat weaker, because here strong cooling flows are suppressed by some non-gravitational heating source. Nevertheless, this shows that CR populations injected from supernovae shocks on galactic scales and by structure formation shocks reinforce the cooling flow problem in contemporary simulations rather than solving it. CRs from supernovae shocks that are injected near the cluster centre could have in principle triggered convective instabilities in the lighter relativistic CR component, but this effect is not really seen in our simulations.

The dynamical state of the cluster crucially determines the relative CR pressure X_{CR}: (1) In the case of ongoing merger activity, the relative CR pressure is boosted due to strong merger shock waves that effectively inject CRs and mix the highly CR-enriched intergalactic medium outside clusters with the ICM. (2) In a post-merger state, weak virialisation shocks traversing the cluster after the merger thermalize random gas motions, thereby increasing the thermal energy and yielding a decrease of X_{CR}. CR loss processes and adiabatic compression furthermore decrease X_{CR} in intermediate cluster regions with a comparatively long thermal cooling time scale. (3) Small cool core clusters are characterised by a higher value of X_{CR} than more massive clusters, albeit the integrated X_{CR} is significantly reduced compared to our merging systems. This is mainly due to the nature of the virialisation process where weaker shocks are responsible for the energy dissipation in larger systems. This leads to a more efficient CR energy injection in small systems and hence to a smaller value of X_{CR}. Altogether, we observe a strong correlation between merging activity and the level of X_{CR}.

How does a CR component affect thermal cluster observables? We found out that central cluster regions of low-mass clusters are most strongly affected by the CR component which leads to an enhanced central density and thermal pressure. Since the X-ray emission scales as the square of the gas density, the X-ray luminosity in low mass clusters of our CR simulations is boosted by up to $\Delta L_X/L_X \simeq 40$ per cent. The amplitude of the thermal Sunyaev-Zel'dovich effect is also modified by CR feedback. While the central Compton-y parameter in these systems is increased by $\Delta y_0/y_0 \simeq 25$ per cent, the integrated Sunyaev-Zel'dovich effect appears to be remarkably robust and the total flux decrement only slightly reduced by typically 2 per cent. In merging clusters, the

sign and the magnitude of the CR-induced effects are quite irregular due to the merger induced inhomogeneities in the ICM.

REFERENCES

Aharonian F., et al. 2006, Nature, 439, 695

Balogh M. L., Pearce F. R., Bower R. G., Kay S. T., 2001, MNRAS, 326, 1228

Benson A. J., Lacey C. G., Baugh C. M., Cole S., Frenk C. S., 2002, MNRAS, 333, 156

Blandford R., Eichler D., 1987, Phys. Rep., 154, 1

Borgani S., Dolag K., Murante G., Cheng L.-M., Springel V., Diaferio A., Moscardini L., Tormen G., Tornatore L., Tozzi P., 2006, MNRAS, 367, 1641

Borgani S., Murante G., Springel V., Diaferio A., Dolag K., Moscardini L., Tormen G., Tornatore L., Tozzi P., 2004, MNRAS, 348, 1078

Cen R., 2005, ApJ, 620, 191

Chandran B. D. G., 2004, ApJ, 616, 169

Dolag K., Vazza F., Brunetti G., Tormen G., 2005, MNRAS, 364, 753

Drury L. O., 1983, Reports of Progress in Physics, 46, 973

Dubinski J., Humble R. J., Loken C., Pen U.-L., Martin P. G., 2003, in Proc. of the 17th Annual International Symposium on High Performance Computing Systems and Applications: McKenzie: A Teraflops Linux Beowulf Cluster for Computational Astrophysics

Eke V. R., Cole S., Frenk C. S., 1996, MNRAS, 282, 263

Ellison D. C., Eichler D., 1984, ApJ, 286, 691

Enßlin T. A., Pfrommer C., Springel V., Jubelgas M., 2006, submitted to A&A

Ettori S., Dolag K., Borgani S., Murante G., 2006, MNRAS, 365, 1021

Evrard A. E., 2004, in Mulchaey J. S., Dressler A., Oemler A., eds, Clusters of Galaxies: Probes of Cosmological Structure and Galaxy Evolution: Galaxy Clusters as Probes of Cosmology and Astrophysics. p. 1

Haardt F., Madau P., 1996, ApJ, 461, 20

Hernquist L., Katz N., 1989, ApJS, 70, 419

Jubelgas M., Springel V., Enßlin T. A., Pfrommer C., 2006, submitted to A&A

Kang H., Jones T. W., 1995, ApJ, 447, 944

Kang H., Jones T. W., 2005, ApJ, 620, 44

Kang H., Jones T. W., Gieseler U. D. J., 2002, ApJ, 579, 337

Katz N., Weinberg D. H., Hernquist L., 1996, ApJS, 105, 19

Katz N., White S. D. M., 1993, ApJ, 412, 455

Kravtsov A. V., Nagai D., Vikhlinin A. A., 2005, ApJ, 625, 588

Malkov M. A., O'C Drury L., 2001, Reports of Progress in Physics, 64, 429

Miniati F., 2001, Computer Physics Communications, 141, 17

Miniati F., Ryu D., Kang H., Jones T. W., 2001, ApJ, 559, 59

Miniati F., Ryu D., Kang H., Jones T. W., Cen R., Ostriker J. P., 2000, ApJ, 542, 608

Navarro J. F., Hayashi E., Power C., Jenkins A. R., Frenk C. S., White S. D. M., Springel V., Stadel J., Quinn T. R., 2004, MNRAS, 349, 1039

Pfrommer C., Enßlin T. A., 2003, A&A, 407, L73

Pfrommer C., Enßlin T. A., 2004, A&A, 413, 17

Pfrommer C., Springel V., Enßlin T. A., Jubelgas M., 2006, MNRAS, 367, 113

Rybicki G. B., Lightman A. P., 1979, Radiative processes in astrophysics. New York, Wiley-Interscience

Ryu D., Kang H., 2003, Journal of Korean Astronomical Society, 36, 105

Ryu D., Kang H., 2004, Journal of Korean Astronomical Society, 37, 477

Ryu D., Kang H., Hallman E., Jones T. W., 2003, ApJ, 593, 599

Salpeter E. E., 1955, ApJ, 121, 161

Sarazin C. L., 1988, X-ray emission from clusters of galaxies. Cambridge Astrophysics Series, Cambridge: Cambridge University Press, 1988

Sijacki D., Springel V., 2006, MNRAS, 366, 397

Spitzer L., 1978, Physical processes in the interstellar medium. New York Wiley-Interscience, 1978

Springel V., 2005, MNRAS, 364, 1105

Springel V., Hernquist L., 2002, MNRAS, 333, 649

Springel V., Hernquist L., 2003, MNRAS, 339, 289

Springel V., Yoshida N., White S. D. M., 2001, New Astronomy, 6, 79

Sunyaev R. A., Zeldovich Y. B., 1972, Comments on Astrophysics and Space Physics, 4, 173

Tormen G., Bouchet F. R., White S. D. M., 1997, MNRAS, 286, 865

Voit G. M., 2005, Reviews of Modern Physics, 77, 207

Yoshida N., Sheth R. K., Diaferio A., 2001, MNRAS, 328, 669

APPENDIX A: SCHWARZSCHILD CRITERION FOR CONVECTIVE STABILITY

This section follows the derivation by Chandran (2004) and derives a dimensionless criterion for convective stability in the presence of a composite fluid of thermal gas and CRs. Consider a parcel of thermal gas and CRs initially at a distance $r = r_0$ from the cluster centre. The parcel is displaced by a radial distance Δr to $r = r_1 = r_0 + \Delta r$. For simplicity thermal conduction and CR diffusion into and out of the parcel are neglected so that the parcel expands adiabatically from the gas density ρ to ρ'. At the final stage, the parcel is mixed with its surroundings. The volume occupied by the thermal gas and that occupied by the CRs expands by the same amount, implying

$$\frac{\rho'}{\rho_0} = \frac{\rho'_{CR}}{\rho_{CR,0}} = 1 + \delta. \qquad (A1)$$

The values of ρ, P_{th}, and P_{CR} in the parcel initially at the same average values at $r = r_0$ which are denoted by ρ_0, $P_{th,0}$, and $P_{CR,0}$. After the parcel is displaced radially outward, the new fluid quantities within the parcel are denoted ρ', P'_{th}, and P'_{CR}. The average fluid quantities (outside the parcel) at $r = r_1$ are denoted ρ_1, $P_{th,1}$, and $P_{CR,1}$. The total pressure is given by the sum of the partial pressures and denoted without any subscript, $P = P_{th} + P_{CR}$. The difference between the thermal gas density in the displaced parcel and its surroundings at $r = r_1$ is denoted by $\Delta\rho = \rho' - \rho_1$. Other

fluid quantities such as the thermal pressure are denoted similarly, $\Delta P_{\rm th} = P'_{\rm th} - P_{\rm th,1}$, etc. Since the parcel expands adiabatically, we have

$$P'_{\rm th} = P_{\rm th,0}\,(1 + \delta)^{\gamma_{\rm th}} \qquad \text{and} \qquad P'_{\rm CR} = P_{\rm CR,0}\,(1 + \delta)^{\gamma_{\rm CR}}. \qquad (A2)$$

Assuming that the turbulent velocities are subsonic, the total pressure inside the parcel approximately matches the average value outside the parcel, $P_1 = P'$. We assume a small displacement $|\Delta r| \ll r$ and expand the average values of the density and the pressure outside the parcel at $r = r_1$ into their Taylor series,

$$\rho_1 \simeq \rho + \frac{d\rho}{dr}\,\Delta r \qquad \text{and} \qquad P_1 \simeq P + \frac{dP}{dr}\,\Delta r. \qquad (A3)$$

Employing adiabatic expansion of the total pressure within the parcel (Eqn. A2), to lowest order in $\Delta r/r$ we arrive at the following set of equations,

$$\delta \;=\; \frac{1}{\gamma_{\rm eff}\,P}\frac{dP}{dr}\,\Delta r, \qquad (A4)$$

$$\frac{\Delta\rho}{\rho} \;=\; \left(\frac{1}{\gamma_{\rm eff}\,P}\frac{dP}{dr} - \frac{1}{\rho}\frac{d\rho}{dr}\right)\Delta r, \qquad (A5)$$

$$\frac{\Delta A}{A} \;=\; \left(\frac{1}{P}\frac{dP}{dr} - \frac{\gamma_{\rm eff}}{\rho}\frac{d\rho}{dr}\right)\Delta r. \qquad (A6)$$

Here, we introduced for convenience the effective adiabatic index of the composite fluid,

$$\gamma_{\rm eff} \equiv \frac{d\log(P_{\rm th} + P_{\rm CR})}{d\log\rho} = \frac{\gamma_{\rm th}P_{\rm th} + \gamma_{\rm CR}\,P_{\rm CR}}{P_{\rm th} + P_{\rm CR}}, \qquad (A7)$$

and the effective entropic function $A = (P_{\rm th} + P_{\rm CR})\rho^{-\gamma_{\rm eff}}$. Since we kept only the lowest orders, it is not necessary to specify in Eqns. (A4) to (A6) whether the hydrodynamic quantities are evaluated at r_0 or r_1, and hence we dropped the subscripts on ρ, P, etc. Since the displacement Δr is a signed quantity, the criterion for convective stability is

$$\frac{\Delta\ln A}{\Delta r} > 0. \qquad (A8)$$

For negligible CR pressure contribution, this criterion is equivalent to the classical Schwarzschild criterion

$$\frac{\Delta\ln A_{\rm th}}{\Delta r} > 0. \qquad (A9)$$

Interestingly, the ICM can be convectively unstable even when the specific entropy of the thermal gas increases outward, as long as $dP_{\rm CR}/dr$ is negative and its absolute value is sufficiently large!

This paper has been typeset from a TeX/ LaTeX file prepared by the author.